



KING'S COLLEGE LONDON
DEPARTMENT OF PHYSICS

Kinetic Monte Carlo Simulation of Screw Dislocations in Iron

Author:

Omar Al-lahham

Supervisor:

Prof. Tony Paxton

A thesis submitted for the degree of

MSc in Physics

5th October 2020

Abstract

A kinetic Monte Carlo model for simulating the three-dimensional motion of dislocations in body-centred-cubic metals with a focus on iron is introduced. It is shown that the model produces results that are both consistent with theory and with those in the literature, with a particular focus on two reference sources. In one case the model shows that there is an error in the reference data, which is confirmed by analysis with theoretical equations. This model has been coded in the Python programming language by the author of this report and is available at github.com.

Acknowledgements

Firstly I would like to thank Professor Tony Paxton for giving me the opportunity to continue my studies at PhD level. Secondly, I should thank my wife Sitti for putting up with me talking about “kinetic Monte Python” for the better part of a year! Also, thanks to Tigany Zarrouk for his help on the computers, and, finally, thanks to Beryl, Opal and Tar, without whom this report wouldn’t have been possible!

Contents

1	Introduction	1
1.1	Overview and Objectives	1
1.2	The Kinetic Monte Carlo Method	3
1.3	Dislocations	6
1.3.1	Geometric Properties	6
1.3.2	Dislocation Movement	9
1.4	Slip in Body-centred-cubic Crystals	11
2	Thermal Activation	13
2.1	Activation Energy and Activation Volume	13
2.2	The Peierls Mechanism	14
2.2.1	Line Tension Model	15
2.2.2	Elastic Interaction Model	23
2.2.3	Model Validity	24
2.2.4	Kocks' Law	25
2.3	The Frequency Prefactor	26
3	The Kinetic Monte Carlo Model	29
3.1	Previous Studies	29
3.2	Implementation	34
3.3	Dislocation Velocity	37
4	Results and Discussion	39
4.1	Comparison with Reference Data I	39
4.2	Comparison with Reference Data II	43
4.3	General	48
5	Summary and Outlook	51
	Bibliography	60

Chapter 1

Introduction

1.1 Overview and Objectives

For centuries iron and civilisation have been inextricably linked, and with global steel production exceeding 1.8 billion tonnes in 2019^[1], this relationship shows little sign of weakening. Of the body-centred cubic (bcc) metals, then, iron is probably the most important to our society, and a better understanding of how it plastically deforms will be helpful in the design of stronger, more resilient alloys of this material and will also allow more accurate predictions to be made regarding the longevity of components made from such alloys.

Central to the understanding of how crystalline materials such as iron plastically deform is the role of line defects known as dislocations^[2]. The *glide* of these defects under applied stress results in the slip of crystallographic planes of atoms over one another, with this process of slip being the main mode of plastic deformation in these materials. The motion of a dislocation is accomplished by the breaking and reconfiguring of those atomic bonds immediately around its line. This necessitates an atomistic approach to accurately account for the processes occurring in this *core* region, which is typically a few interatomic spacings in size, around the dislocation line. Electronic structure (ES) calculations and molecular dynamics (MD) simulations are used for this purpose; however, because of the limited system sizes (ES up to ~ 1000 atoms) and time scales (up to $\sim \mu\text{s}$) associated with these simulation methods, their results are not directly comparable with experiment. In general, dislocation motion occurs over relatively longer time scales, which can include *rare*

thermally activated events.

To help bridge this gap between the experimental and the atomistic, results from atomistic calculations are used to parameterise elastic continuum^[3] approaches to dislocation modelling. One of these approaches is dislocation dynamics (DD)^[4,5], in which dislocation networks are represented by nodes connected by straight line segments. Dislocation motion is treated as deterministic, with nodal forces and the velocities in response to these forces being calculated. This approach is capable of simulating much larger systems, closer to experimental sizes and time scales (\sim s)^[6], limited in reliability only by how accurately the nodal velocities are calculated in response to the forces.

The single most important input to a DD simulation is dislocation velocity as a function of stress and also of temperature; i.e. mobility rules. Although mobility rules can be extracted directly from atomistic simulations, they can also be provided by another elastic continuum approach, which also represents dislocations by interconnected straight line segments. Unlike DD, however, this approach is stochastic, utilising the kinetic Monte Carlo (kMC) method^[7-9].

Simulations utilising the kMC method evolve through a sequence of elementary events, which are randomly chosen with a probability proportional to the event's rate of occurrence. Atomistic information is incorporated by expressing the event rates in terms of their respective energy barriers. The advantage of this approach is that any experimental time scale can be achieved. This is due to both the fact that the simulation time-step, although stochastic, depends on the reciprocal of the sum of the rates of each possible event calculated at each iteration and that each event is associated with a system transition between metastable states. The latter fact also makes this approach more computationally efficient than MD, as phase trajectories around energy minima are neglected. Another difference with DD is that, although, in general, only one dislocation is simulated at a time, finer detail is resolved along the dislocation line so that complicated interactions between short line segments known as *kinks* (this will be described in more detail in the following sections) are included.

Taking into account kink interactions together with the fact that the dynamics of the dislocation line can be tracked over much longer time-scales, means that

more accurate mobility rules can be extracted for use in DD simulations than those extracted directly from atomistic simulations. However, dislocation simulations utilising the kMC method are not only useful for extracting mobility rules for DD simulations. The velocity data obtained from them are valuable in their own right; e.g. for calculating the plastic strain rate of a material using the Orowan equation^[10] and particularly for predicting regimes of solid solution softening or hardening under different levels of temperature, applied stress and solute concentration^[11-13].

The aim of this research project has been to develop a kMC code that simulates the motion of a screw dislocation in a perfect bcc lattice of iron (α -Fe). The motion is three-dimensional, on intersecting $\{110\}$ planes, which allows complicated kink interactions to occur. This code has been written in the Python programming language. The results of simulations using this code are presented in this report, and it's shown that this code produces results that are both consistent with those in the literature and with the predictions of theoretical equations. This work forms the basis for future research in this area in which carbon will also be included in the model, needing only parameterisation from atomistic calculations to do so. This code can also be easily adapted for other bcc metals.

The structure of this report is as follows. In Chapter 2 the relevant theory that the model describes will be developed, followed by a discussion of previous works and the model implementation in Chapter 3. In Chapter 4 the results will be presented and discussed, and the report is concluded in Chapter 5. The remainder of this Chapter will describe the kMC method followed by an introduction to dislocation theory and slip in bcc materials.

1.2 The Kinetic Monte Carlo Method

Monte Carlo methods, such as those based on the Metropolis algorithm^[14], sample a system's equilibrium distribution, and time has no physical meaning in such simulations. In contrast, although random numbers are also used to generate a random sequence of moves, a kMC simulation evolves a system dynamically in real time. This time evolution is course-grained, being the time that the system spends in energy minima between transitions between them, with these transitions being

rare (and too slow to be observed on the time scales of atomistic simulations) if the energy barriers are larger than the available thermal energy ($k_B T$).

The kMC method is best applied to situations where a system evolves stochastically through a succession of elementary events where there are only a few possible event types. The thermally activated motion of a dislocation is just such a situation for which the kMC method is well suited to model, as this motion can be broken down into just three elementary events: *kink-pair nucleation*, *kink migration* and *kink annihilation*, which are described as follows. Thermal fluctuations can cause a short segment of the dislocation line to advance over to the next potential valley of the periodic lattice potential, creating a pair of oppositely signed kinks in the process, which straddle the potential hill between the valleys. This process of kink-pair nucleation is illustrated in Figure 1.1.

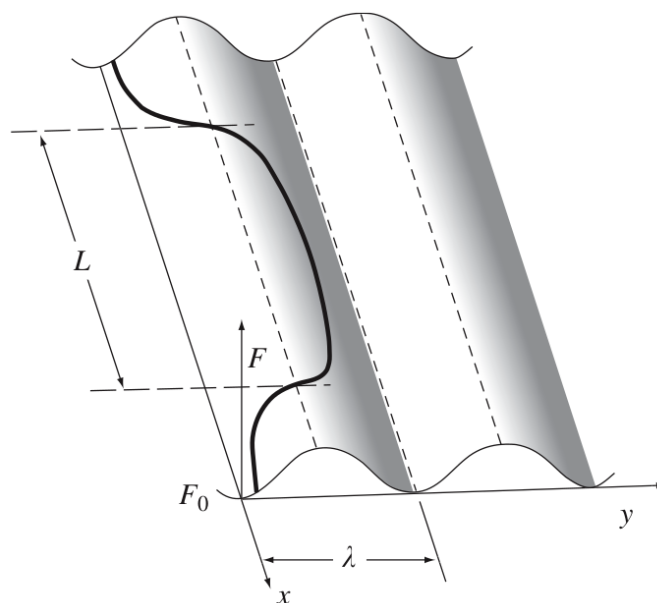


Figure 1.1: Illustrating the nucleation of a kink-pair. F represents the lattice potential, F_0 the dislocation free energy along the potential valley, L is the kink-pair width and λ is the distance between potential valleys^[15].

The kink-pair may then either annihilate, i.e. recombine after being pulled toward each other due to their mutual elastic attraction, or they may migrate, moving apart with the assistance of thermal fluctuations and/or stress, eventually pulling all of the dislocation line into the next potential valley.

Now, the occurrence rates J of these events are expressed as the product of a

frequency pre-factor (an attempt frequency) f and a Boltzmann factor:

$$J = f \exp\left(-\frac{\Delta G(\tau, T)}{k_B T}\right), \quad (1.1)$$

where k_B is Boltzmann's constant and T is the absolute temperature. ΔG is the Gibbs free energy of activation, which can be determined through atomistic calculations, and it's in general a function of stress τ and temperature T . It's the energy that must be supplied by thermal fluctuations at constant temperature and stress and, following the convention of Schoeck^[16] and Kocks *et al*^[17], it's defined as

$$\Delta G = \Delta F - \Delta W, \quad (1.2)$$

where ΔF is the Helmholtz free energy difference between that of the saddle point and that of the ground state and ΔW is the work done by the applied stress. If $\Delta W = 0$, then ΔG would be the difference between the potential peak and F_0 in Figure 1.1; though, the saddle configuration of the dislocation changes with the applied stress.

The frequency prefactor f could be determined using harmonic transition state theory (HTST)^[18]; however, even this approximation is computationally expensive for large systems. In the literature, this prefactor is either estimated^[6,12,13,19-21] or fitted to experimental data^[11], with values used being found between 10^9 and 10^{13} s^{-1} .

The event occurrence/transition rates are completely determined by the configuration of the dislocation line at each kMC time step, making the random sequence of dislocation configurations produced by the transitions a *Markov chain*. Given a particular dislocation configuration, the total rate of escape R from this state is given by

$$R = \sum_{\alpha, i} J_{\alpha, i}, \quad (1.3)$$

where α represents the event type and i the particular dislocation segment. The residence time Δt in this state is a random variable that satisfies the exponential distribution: $p(\Delta t) = R e^{-R \Delta t}$. By selecting a random number q uniformly distributed

in the range $[0, 1)$, we can obtain[†] $\Delta t = -R^{-1} \ln(1 - q)$.

So, at each time step of the kMC simulation the transition rates for each segment of the dislocation line are calculated and a residence time is randomly selected, which depends on the total transition rate R . Which of the total number of events is chosen depends on its contribution to R , and this is done by applying the method introduced by Bortz, Kalos, and Lebowitz^[7], which is detailed in the following algorithm that summarises a general kMC simulation.

The kMC Algorithm

1. Initialise the simulation. Set the time $t := 0$.
2. Calculate and form a list of all of the rates J_i of all possible transitions available to the current state of the system.
3. Calculate the cumulative function $S_k := \sum_{i=1}^k J_i$ for $i = 1, \dots, N$, where N is the total number of available transitions. Denote $R := S_N$.
4. Draw a random number q_1 uniformly distributed in $[0, 1)$ and then update the time $t := t + \Delta t$, where $\Delta t := -R^{-1} \ln(1 - q_1)$
5. Draw another random number q_2 uniformly distributed in $[0, 1)$ and find the event k to carry out by finding the k for which $S_{k-1} < Rq_2 \leq S_k$, where $S_0 = 0$.
6. Carry out the event k .
7. If the maximum number of iterations is reached, stop. Otherwise, return to step 2.

This algorithm is known as the *residence-time algorithm* or the *n-fold way*.

1.3 Dislocations

1.3.1 Geometric Properties

A dislocation is defined by two vectors: a *line direction* $\boldsymbol{\xi}$ and a *Burgers vector* \mathbf{b} . The Burgers vector of a dislocation quantifies the amount of crystal distortion caused by its presence, and for the non-dissociated dislocations that are considered in this work, it is always a lattice translation vector. If we consider a crystal containing

[†]Since $\int_0^\infty p(t) dt = 1$, then for q we have $q = \int_0^{\Delta t} p(t) dt$. Integrating and then inverting the result yields $\Delta t = -\ln(1 - q)/R$. Also, $\langle t \rangle = \int_0^\infty tp(t) dt = 1/R$.

a dislocation as a deformed continuum body, then, using the displacement field \mathbf{u} , which relates the deformed configuration of the crystal with the undeformed configuration (without the dislocation), the Burgers vector can be defined by the line integral

$$\mathbf{b} = \oint_C d\mathbf{u}, \quad (1.4)$$

where C is any closed curve in the crystal around the dislocation line. If C enclosed several dislocations, then the integral would give the vector sum of their Burgers vectors. This integral being non-zero expresses the fact that the displacement field \mathbf{u} in a crystal with a dislocation must be discontinuous or multivalued. This is the case as the atoms of such a distorted crystal cannot be brought into one-to-one correspondence with the atoms of the same crystal without the dislocation.

Now, dislocations can be classified into two primary types according to the angle between their line direction and Burgers vector: *edge dislocations*, which have $\mathbf{b} \cdot \boldsymbol{\xi} = 0$, and *screw dislocations*, such as the one modelled in this work, which have $\mathbf{b} \cdot \boldsymbol{\xi} = \pm|\mathbf{b}| = \pm b$. For edge dislocations, this relation defines a unique plane on which they are constrained to glide. Screw dislocations, however, are not restricted in this way, and are free, in principle, to glide on any plane, being able to *cross-slip* from one to another depending on the local stress conditions. The kinks on the dislocation modelled in this work, however, are of edge type, and so they are constrained to move on their own glide planes during migration. In general, dislocations found in real materials are of a mixed type, showing the characteristics of both, and so are constrained to move on a single glide plane, due to their edge component.

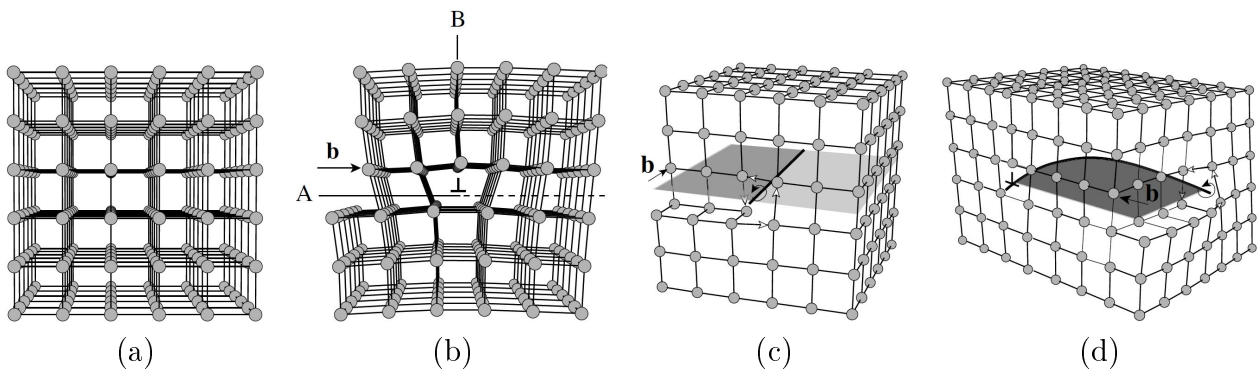


Figure 1.2: (a) A perfect simple cubic crystal. (b) Creation of an edge dislocation \perp by shearing the top half of the perfect crystal along the half plane A (solid line). A screw dislocation (c) and a mixed dislocation (d)^[6].

Figure 1.2 shows a perfect simple cubic crystal in (a), and, also in simple cubic crystals, an edge dislocation in (b), a screw dislocation in (c) and a mixed dislocation in (d). The edge dislocation in (b), which is indicated by \perp , has been formed by shearing the top half of the perfect crystal over the half plane A, which is indicated by the solid line. The dislocation is situated at the *edge* of an extra half-plane of atoms B, and its line (perpendicular to the plane of the figure) is the boundary between the slipped portion and the unslipped portion (indicated by the dashed line) of the crystal. As can be seen, \mathbf{b} is perpendicular to the dislocation line and is a lattice translation vector. An edge dislocation could also be formed by the condensation of interstitials or vacancies (extra atoms in the lattice or empty atomic sites).

A screw dislocation is called as such as the atoms around the dislocation line are arranged in a spiral. This is shown in Figure 1.2(c) by the arrows around the solid line. The figure also shows that the dislocation line still forms the boundary between the slipped (dark grey) and unslipped (light grey) portions of the crystal and that \mathbf{b} is a lattice translation vector. However, in contrast to Figure 1.2(b), the shear displacement by \mathbf{b} of the top half of the crystal with respect to the bottom half is now parallel to the dislocation line rather than perpendicular to the dislocation line.

Figure 1.2(d) shows a mixed dislocation. The mixed dislocation begins with edge character (on the left), ends with screw character, and at intermediate points it can be resolved into edge and screw components using the angle between the dislocation line and \mathbf{b} . Now, the amount of crystal distortion on the surface bounded by the dislocation line (dark grey) is constant. Therefore, \mathbf{b} must be the same at all points along the dislocation line – it's an intrinsic property of it.

Finally, two dislocations with the same line direction but opposite Burgers vectors are physical opposites, and would annihilate, restoring a perfect crystal, if brought together. This is the case for the kink and the antikink in a kink-pair. Also, a dislocation cannot begin or end inside a crystal; it must either intersect a free surface, form a closed loop or branch into other dislocations.

1.3.2 Dislocation Movement

Glide and Climb

As mentioned earlier, dislocations glide under applied stress. Glide is when a dislocation moves in a plane that contains both its line and Burgers vector (its glide plane), and this type of motion is conservative, as the number of atoms and lattice sites is conserved. Edge dislocations glide in the direction of (crystal) slip \mathbf{b} , whereas screw dislocations glide perpendicular to \mathbf{b} ; though the direction of slip is still \mathbf{b} . The glide of many dislocations results in the slip of crystallographic planes of atoms over one another, the manifestation of which is the formation of steps on the surface of a crystal. The direction of slip (which is given by \mathbf{b}) corresponds to one of the shortest lattice translation vectors, and this is usually the direction along which the atoms are the most closely spaced, whereas glide planes tend to be those with the largest interplanar spacing.

Another form of dislocation motion is climb, which is when a dislocation moves out of its glide surface, perpendicular to its Burgers vector. This is a non-conservative form of motion, as material has to be added or removed for it to take place. For example, if the row of atoms directly above the edge dislocation in Figure 1.2(c) was to be removed, then the dislocation would climb upwards. Pure screw dislocations have no extra half-plane and so, in principle, cannot climb.

In this work, the focus is on glide motion, which occurs much more readily than climb under typical mechanical conditions, and so is the dominant form of dislocation mediated plastic deformation. Consequently, dislocations are typically characterised by their Burgers vector and glide plane, and for the type of screw dislocations considered in this work this is written as $\frac{1}{2}\langle 111 \rangle \{110\}$.

The CRSS, Schmid's Law and the Peierls Stress

Consider Figure 1.3 in which a cylindrical crystal is being deformed in tension by a uniaxial force F . The shear stress resolved on the slip-plane in the slip direction, τ , is given by

$$\tau = \frac{F}{A} \cos \phi \cos \lambda, \quad (1.5)$$

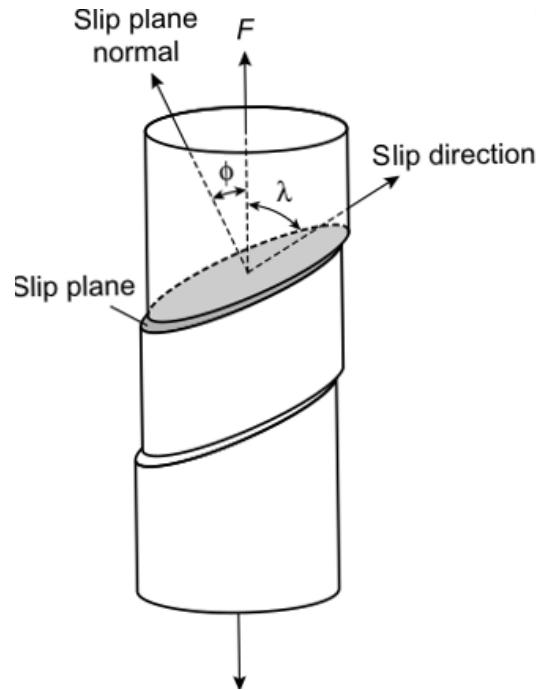


Figure 1.3: Illustration of the geometry of slip^[22].

where A is the cross-sectional area of the crystal. The value of τ required to initiate slip/dislocation glide is known as the *critical resolved shear stress* or the CRSS. For such a uniaxial deformation of a crystal (tension or compression), Schmid's law states that, irrespective of the crystal orientation, glide sets in at that axial stress F/A at which the resolved shear stress reaches this critical value^[23]. A corollary of this is that if there are a set of crystallographically equivalent slip systems such as the bcc $\langle 111 \rangle \{110\}$ systems on which the type of screw dislocations modelled in this work glide, then the first one to be activated under such uniaxial deformation will be the one where the Schmid factor, i.e. $\cos \phi \cos \lambda$, is closest to $1/2$ ^[24].

The minimum value of the CRSS would apply to a single dislocation in an otherwise perfect crystal, and in the low temperature limit this stress is referred to as the *Peierls stress* τ_p ; i.e. the minimum stress required to initiate dislocation glide at zero temperature. The Peierls stress can be obtained from the maximum derivative of the *Peierls potential*, i.e. the periodic lattice potential mentioned earlier, with respect to a dislocation line's position; though, this assumes that the dependence of the Peierls potential on the applied stress tensor can be neglected^[25,26].

Finally, under zero applied stress, the energy barrier (per unit length) to dislocation glide motion is known as the *Peierls barrier* (the difference between F_0 and the potential peak in Figure 1.1), and as mentioned earlier, this can be surmounted with

the aid of thermal fluctuations by the nucleation and subsequent lateral relaxation of kink-pairs, even if the applied stress field is less than τ_p . This kink-pair mechanism of dislocation motion is often also referred to as the *Peierls mechanism*.

The Peach-Koehler Force

The force \mathbf{f} acting on a unit line element of a dislocation due to an external stress field described by the tensor $\boldsymbol{\tau}$ is given by the Peach-Koehler formula^[27]:

$$\mathbf{f} = (\mathbf{b} \cdot \boldsymbol{\tau}) \times \boldsymbol{\xi}, \quad (1.6)$$

such that glide forces always act perpendicularly to the dislocation line.

1.4 Slip in Body-centred-cubic Crystals

The plasticity of bcc metals depends strongly on temperature and strain rate below a critical temperature that is around 10–25% of the melting point. This temperature and strain rate dependence is caused by the thermally activated motion of $\frac{1}{2}\langle 111 \rangle$ screw dislocations, which proceeds by means of the Peierls mechanism^[28,29].

The mobility of $\frac{1}{2}\langle 111 \rangle$ screw dislocations is severely limited by a non-planar core, which spreads symmetrically on to three $\{110\}$ planes of the $\langle 111 \rangle$ zone^[30–33]. This, spreading in a sense, “anchors” the core, and it must undergo a transformation to a glissile configuration before slip can begin, which means that the activation energy for kink-pair nucleation is relatively high. In contrast, non-screw dislocations of the same Burgers vector are highly mobile and move with velocities that scale linearly with the applied stress. This is because they have a planar core structure, and so no transformation of the core is required to initiate glide, which can thus begin at much lower (Peierls) stresses than those of the screw dislocation^[28,34].

Dislocations in fcc and other close-packed metals where atoms can easily be shifted with respect to each other also have planar cores. They therefore also have low Peierls stresses and activation energies for kink-pair nucleation, which means that the Peierls mechanism is restricted to temperatures close to 0K in these crystals and that their plasticity is only very weakly temperature dependent^[35,36].

The slip direction in bcc crystals is well established to be $\langle 111 \rangle$ and it is now

generally accepted that the elementary slip planes are $\{110\}$. That the slip planes are $\{110\}$ is evident at very low temperatures where this almost always observed to be the case, with the slip being planar. However, at higher temperatures slip becomes non-planar, with slip traces becoming increasingly wavy and diffuse, and slip activity seemingly being observed on $\{112\}$ and $\{123\}$ planes^[29]. More recent experiments^[37–39] and atomistic and DD results^[40–43], though, show that the slip seemingly being observed on other planes is composed of elementary steps on $\{110\}$ planes only, of which there are three that intersect any $\langle 111 \rangle$ direction. Which average plane that slip is observed on is a compromise between the maximum-resolved-shear-stress (MRSS) plane (which may not be a lattice plane) and a close-by plane of low resistance to dislocation motion.

Another contrast with fcc metals (and most other close packed metals) is the breakdown of Schmid’s law in bcc metals. One manifestation of this is that the CRSS to make a screw dislocation glide along $[111]$ or $[\bar{1}\bar{1}\bar{1}]$ directions on average $\{112\}$ planes is not equal. This is due to the fact that the $\{111\}$ planes are not mirror planes in the bcc lattice – the so called *twinning-antitwinning asymmetry*. A related effect is tension-compression asymmetry, where the critical stresses for tension and compression are different for the same loading orientation^[44]. The former two non-Schmid effects are *intrinsic* effects, which are a property of the bcc lattice. Another deviation from Schmid’s law is that components of the applied stress tensor that do not exert any glide force on the dislocation can also affect the CRSS required to initiate glide. This is an *extrinsic* non-Schmid effect, and it’s another consequence of the spreading of the screw dislocation’s core, which allows it to be modified by stresses both parallel and perpendicular to the slip direction^[26,40,44,45].

In summary, the non-planar core structure of the $\frac{1}{2}\langle 111 \rangle$ screw dislocations leads to a large intrinsic lattice friction, which makes the plasticity of bcc materials strongly temperature dependent, and it also allows it to be affected by non-glide stresses, a manifestation of which is wavy and diffuse (non-Schmid) glide at higher temperatures. Lastly, the mirror asymmetry of the bcc lattice about $\{111\}$ planes leads to the intrinsic non-Schmid effects of twinning-antitwinning asymmetry and tension-compression asymmetry.

Chapter 2

Thermal Activation

In this chapter thermal activation as applied to the motion through the kink-pair/Peierls mechanism of $\frac{1}{2}\langle 111 \rangle$ screw dislocations in bcc materials will be reviewed. Firstly, the concept of *activation volume* will be introduced. Next, the Peierls mechanism will be analysed through two simple models and a phenomenological formula that describes the stress dependence of the activation energy for kink-pair nucleation will be introduced. Lastly, the frequency prefactor for the kMC event rates (Equation (1.1)) will be discussed.

2.1 Activation Energy and Activation Volume

As stated in Section 1.1, the Gibbs free energy of activation ΔG is the energy that must be supplied by thermal fluctuations at constant temperature and stress, and it's given by

$$\Delta G = \Delta F - \Delta W = \Delta U - T\Delta S - \tau b\Delta A, \quad (2.1)$$

where ΔU and ΔS are the internal energy and entropy changes, respectively. The term $\tau b\Delta A$ is the work done by the applied stress τ (resolved in the glide plane), where ΔA is the area swept out by a dislocation during the nucleation of a kink-pair; i.e. the difference between the area enclosed by the dislocation when the kink-pair is in the saddle (unstable equilibrium) configuration and that before the nucleation of the kink-pair (stable equilibrium). It's known as the *activation area* and $b\Delta A = V$ the *activation volume*, and they are experimentally measurable quantities^[15,17,46].

The activation volume is usually defined as

$$V = - \left(\frac{\partial \Delta G}{\partial \tau} \right)_T,$$

which can be seen from

$$\begin{aligned} dG &= dU - d(TS) - d(\tau V) \\ &= TdS + \tau dV - SdT - TdS - Vd\tau - \tau dV \\ &= -SdT - Vd\tau \\ &= \left(\frac{\partial G}{\partial T} \right)_\tau dT + \left(\frac{\partial G}{\partial \tau} \right)_T d\tau, \end{aligned} \tag{2.2}$$

where $dU = TdS + \tau dV$, as work is done on the system by the applied stress.

Another useful relation is

$$\Delta H = \Delta G + T\Delta S = \Delta U - \Delta W, \tag{2.3}$$

where ΔH is the activation enthalpy, and obviously $\Delta H = \Delta G$ when $T = 0$. Now, it has been shown for the case of iron that ΔG is within 5% of ΔH for a broad temperature range^[47]. So, from here on in, the simplifications will be made that

$$\Delta G = \Delta H \quad \text{and} \quad \Delta F = \Delta U. \tag{2.4}$$

2.2 The Peierls Mechanism

The Peierls or kink-pair mechanism, which describes the lattice friction acting on a dislocation, is usually described by two models following Seeger^[48], the applicability of which depend on stress and temperature: a line tension model for a high stress and lower temperature regime, and an elastic interaction model for a low stress and higher temperature regime. These are described as follows, with expressions for the kink-pair activation energies being derived and the validity of the models being discussed.

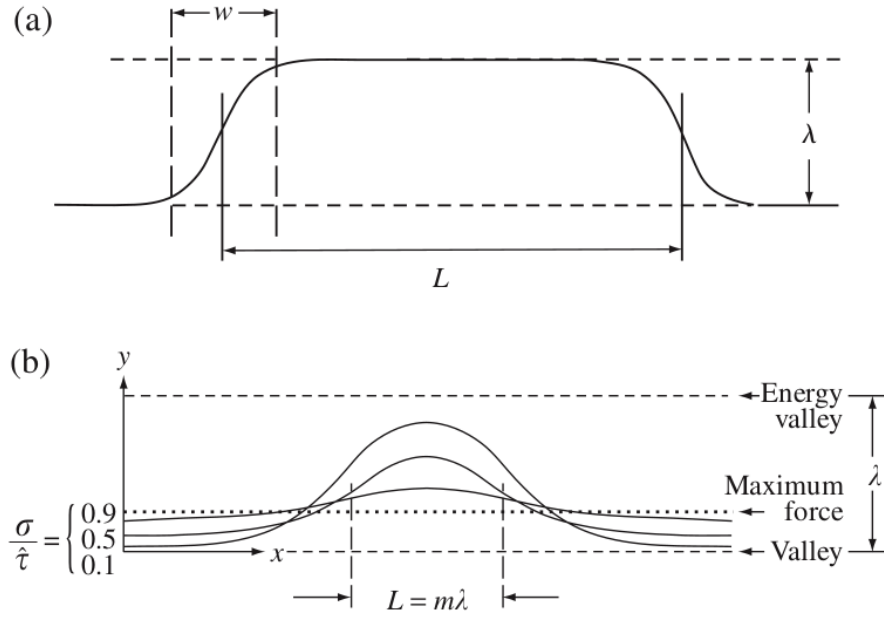


Figure 2.1: “Two limiting forms of idealisation of a double kink on a screw dislocation: (a) at low stresses, where the double kink is made up of two well-separated, fully formed right-side and left-side kinks; (b) at high stresses, where the activation configuration is more in the form of a bulge that just places a portion of the line over the peak of the energy ridge^[15].”

2.2.1 Line Tension Model

In the high stress and lower temperature regime that applies for this model, the saddle configuration of the kink-pair is a bulge where just a portion of the line reaches over the potential ridge/Peierls barrier. This is shown in Figure 2.1(b) for three values of applied stress as a fraction of the Peierls stress (note that in the figure the applied stress resolved in the glide plane is σ and the Peierls stress is $\hat{\tau}$ rather than the τ and τ_p , respectively, which were used earlier), where the x -direction is along the potential/Peierls valley and the dislocation line is mostly aligned along this direction and the y -direction runs between the valleys. As the applied stress increases the dislocation is lifted further from the bottom of the potential/Peierls valley and less of the line reaches over the Peierls barrier. Once the applied stress reaches the Peierls stress (at 0 K), the dislocation line will move in one go across the barrier; i.e. the Peierls mechanism will cease to apply.

Energy of a Critical Bulge

Now, initially following Dorn and Rajnak^[49], in the absence of thermal fluctuations and under an applied stress τ , the dislocation line will be shifted to a position y_0

above the bottom of the Peierls valley. This position is obtained from the balance of forces

$$\tau b = \left. \frac{dU(y)}{dy} \right|_{y=y_0}, \quad (2.5)$$

where $U(y)$ and τb , respectively, represent the Peierls potential and the force due to the applied stress (both per unit length of the dislocation line). The potential term $U(y)$ also includes the energy per unit length of a straight dislocation line lying in a Peierls valley U_0 . The activation enthalpy of the kink-pair/bulge saddle configuration is then given by the excess energy of the bulged line configuration over that of a straight dislocation line lying along y_0 minus the work done by the applied stress:

$$\Delta H = \int_{-\infty}^{\infty} [U(y) ds - (U(y_0) + \tau b(y - y_0)) dx], \quad (2.6)$$

where $ds = \sqrt{dx^2 + dy^2}$ is the length of an infinitesimal segment of the bulged dislocation line. The saddle configuration of the dislocation line can be found using the balance of forces (line tension equilibrium condition)

$$T_L \frac{d^2 y}{dx^2} = \frac{T_L}{2} \frac{d}{dy} \left(\frac{dy}{dx} \right)^2 = \frac{dU(y)}{dy} - \tau b, \quad (2.7)$$

where the first term on the left side is the self stress due to the curvature with line tension T_L . For the smooth model Peierls potentials (Figure 2.2), the boundary conditions for this problem to be satisfied are

$$y = y_0, \quad \frac{dy}{dx} = 0 \quad \text{at} \quad x = \pm\infty, \quad (2.8)$$

$$y = y_s, \quad \frac{dy}{dx} = 0 \quad \text{at} \quad x = 0. \quad (2.9)$$

where y_s is the y -coordinate of the tip of the bulge. Integrating Equation (2.7) gives

$$\frac{T_L}{2} \left(\frac{dy}{dx} \right)^2 = U(y) - \tau b y + C, \quad (2.10)$$

where C is a constant, and integrating again gives

$$x = \pm \sqrt{\frac{T_L}{2}} \int_y^{y_s} (U(y') - \tau b y' + C)^{-1/2} dy', \quad (2.11)$$

where y_s is the constant of integration in this case. From the boundary conditions $x \rightarrow \pm\infty$ as $y \rightarrow y_0$ it can be deduced that $C = -U(y_0) + \tau b y_0$, as the integrand must diverge as $y \rightarrow y_0$, and that the $+$ sign must be taken for $x > 0$ and the $-$ sign for $x < 0$. Equation (2.10) can then be rewritten as

$$\left(\frac{dy}{dx}\right)^2 = \frac{2}{T_L} [U(y) - U(y_0) - \tau b(y - y_0)], \quad (2.12)$$

and from the second boundary condition (2.9), we obtain a relation for y_s :

$$U(y_s) - U(y_0) - \tau b(y_s - y_0) = 0. \quad (2.13)$$

For $y > y_s$, $\frac{dy}{dx}$ is imaginary; i.e. there are no solutions for the tip of the bulge beyond y_s . The physical interpretation of this is that, beyond y_s , the bulge separates into a pair of kinks travelling to $x = \pm\infty$ under the applied stress. For $y < y_s$, $\frac{dy}{dx}$ is discontinuous at $x = 0$, which corresponds to a point force acting on the dislocation in the positive y -direction at $x = 0$, with this force being required to hold the dislocation in position for $y < y_s$ ^[49].

Now, following Caillard and Martin's^[46] line tension (LT) approximation, the integral (2.6) can be written as

$$\Delta H = \int_{-\infty}^{\infty} \left[U(y) \sqrt{1 + \left(\frac{dy}{dx}\right)^2} - U(y_0) - \tau b(y - y_0) \right] dx, \quad (2.14)$$

then using Equation (2.12) and the assumption that $\frac{dy}{dx} \ll 1$ in metals, the integral becomes

$$\Delta H = \int_{-\infty}^{\infty} \left[U(y) \left(1 + \frac{1}{2} \left(\frac{dy}{dx}\right)^2 \right) - U(y_0) - \tau b(y - y_0) \right] dx; \quad (2.15)$$

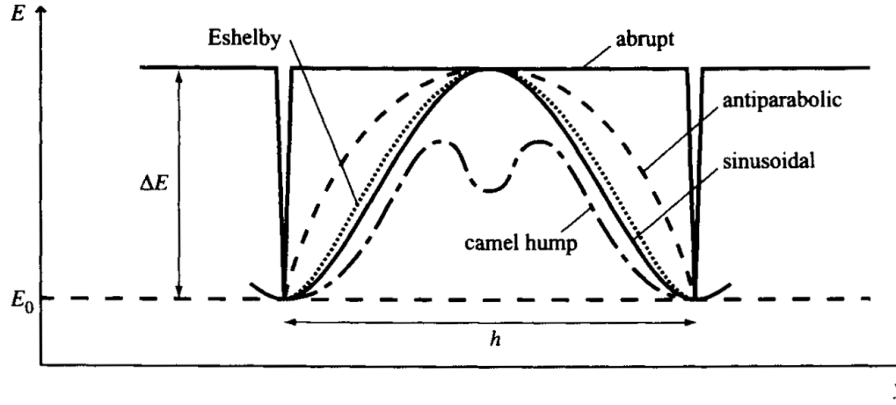


Figure 2.2: Showing some simple model Peierls potentials. (Note that E here is U in the main text.)^[46].

that is,

$$\Delta H = \int_{-\infty}^{\infty} \left[U(y) - U(y_0) - \tau b(y - y_0) + \frac{U(y)}{T_L} [U(y) - U(y_0) - \tau b(y - y_0)] \right] dx, \quad (2.16)$$

and changing the variable gives

$$\Delta H = 2\sqrt{\frac{T_L}{2}} \int_{y_0}^{y_s} \left[\frac{U(y) - U(y_0) - \tau b(y - y_0)}{\sqrt{U(y) - U(y_0) - \tau b(y - y_0)}} + \frac{U(y)}{T_L} \frac{[U(y) - U(y_0) - \tau b(y - y_0)]}{\sqrt{U(y) - U(y_0) - \tau b(y - y_0)}} \right] dy, \quad (2.17)$$

where the factor of 2 comes, as the bulge is symmetric about $x = 0$. Simplifying, using the assumptions that $T_L \approx U_0$ and $U(y) - U(y_0) \ll U_0$, we obtain

$$\Delta H = 2\sqrt{2U_0} \int_{y_0}^{y_s} \sqrt{U(y) - U(y_0) - \tau b(y - y_0)} dy. \quad (2.18)$$

The integral in Equation (2.18) can be solved analytically using the anti-parabolic potential, which is shown in Figure 2.2 along with some other simple model potentials. This potential, which is given by

$$U(y) = U_0 + 4\Delta U \frac{y}{h} \left(1 - \frac{y}{h}\right), \quad (2.19)$$

where ΔU is the height of the Peierls barrier, has its maximum gradient at $y = 0$ such that $\tau_p = 4\Delta U/(hb)$. This leads to the unphysical feature that the dislocation remains trapped in the Peierls valley at $y = 0$ until the Peierls stress is met, with

only the amplitude of the bulge changing with the applied stress. However, it was shown by Argon^[15], by comparison with experimental results, that there is little penalty paid for this feature of the potential, which allows the LT model to be solved analytically.

Expressing the potential (2.19) in terms of τ_p and substituting it into Equation (2.18) leads to

$$\Delta H = \sqrt{\frac{8\tau_p b U_0}{h}} \int_0^{y_s} \sqrt{h \left(1 - \frac{\tau}{\tau_p}\right) y - y^2} dy, \quad (2.20)$$

and from Equation (2.13) it is found that $y_s = h(1 - \tau/\tau_p)$, and so the integral can be rewritten as

$$\Delta H = C \int_0^{y_s} \sqrt{-\left(y - \frac{y_s}{2}\right)^2 + \frac{y_s^2}{4}} dy, \quad (2.21)$$

where $C = \sqrt{8\tau_p b U_0/h}$. This can be solved by use of two substitutions and trigonometric identities:

$$\begin{aligned} \Delta H &= C \int_{y=0}^{y=y_s} \frac{\sqrt{-4u^2 + y_s^2}}{2} du = C \int_{y=0}^{y=y_s} \frac{\sqrt{-y_s^2 \sin^2 v + y_s^2} (y_s \cos v)}{2} dv \\ &= C \int_{-\pi/2}^{\pi/2} \frac{y_s^2}{8} (1 + \cos 2v) dv \\ &= C \frac{y_s^2}{8} \pi; \end{aligned} \quad (2.22)$$

that is,

$$\Delta H = \frac{\pi h^2}{8} \sqrt{\frac{8\tau_p b U_0}{h}} \left(1 - \frac{\tau}{\tau_p}\right)^2 = \frac{\pi h}{\sqrt{2}} \sqrt{\Delta U U_0} \left(1 - \frac{\tau}{\tau_p}\right)^2 \quad (2.23)$$

after using the relations for C , y_s and τ_p . Hence, this is the activation enthalpy of a critical bulge, and it will now be shown that the prefactor to the quadratic term gives the energy of two isolated kinks.

Energy of an Isolated Kink

This derivation follows that of the critical bulge; however, it is simplified due to the absence of a work term. The kinked dislocation line configuration is shown in Figure

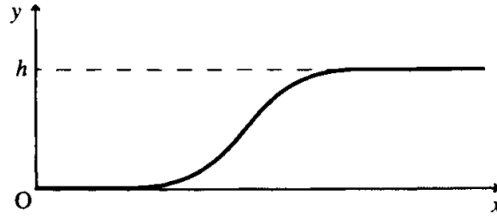


Figure 2.3: “Equilibrium shape of an isolated kink (smooth potential)^[46].”

2.3, and the energy is given by (using $\frac{dy}{dx} \ll 1$ again)

$$U_k = \int_{-\infty}^{\infty} \left[U(y) \left(1 + \frac{1}{2} \left(\frac{dy}{dx} \right)^2 \right) - U_0 \right] dx; \quad (2.24)$$

i.e. the excess energy of the kinked dislocation over that of a straight one lying in a Peierls valley with energy U_0 . The equilibrium line configuration can be found using the LT equilibrium condition once more:

$$\frac{T_L}{2} \frac{d}{dy} \left(\frac{dy}{dx} \right)^2 = \frac{dU(y)}{dy}, \quad (2.25)$$

and the boundary conditions for this problem to be satisfied are

$$y = 0, \quad \frac{dy}{dx} = 0 \quad \text{at} \quad x = -\infty, \quad (2.26)$$

$$y = h, \quad \frac{dy}{dx} = 0 \quad \text{at} \quad x = +\infty. \quad (2.27)$$

Integrating Equation (2.25) and using the boundary conditions gives

$$\frac{T_L}{2} \left(\frac{dy}{dx} \right)^2 = U(y) - U_0, \quad (2.28)$$

and substituting this into Equation (2.24) then changing the variable gives

$$\begin{aligned} U_k &= \int_{-\infty}^{\infty} \left[U(y) \left(1 + \frac{1}{T_L} (U(y) - U_0) \right) - U_0 \right] dx \\ &= \int_0^h \sqrt{\frac{T_L}{2}} \left[\frac{U(y) - U_0 + \frac{U(y)}{T_L} (U(y) - U_0)}{\sqrt{U(y) - U_0}} \right] dy. \end{aligned} \quad (2.29)$$

Using the same assumptions that led to Equation (2.18) and simplifying, we obtain

$$U_k = \sqrt{2}U_0 \int_0^h \sqrt{\frac{U(y)}{U_0} - 1} dy. \quad (2.30)$$

Now, to show that the prefactor in Equation (2.23) gives the energy of two isolated kinks, the anti-parabolic potential (2.19) must be substituted into the equation (though, (2.30) is valid for other potentials):

$$\begin{aligned} U_k &= \sqrt{2}U_0 \sqrt{\frac{4\Delta U}{h^2 U_0}} \int_0^h \sqrt{(hy - y^2)} dy \\ &= \sqrt{2}U_0 \sqrt{\frac{4\Delta U}{h^2 U_0}} \int_0^h \sqrt{-\left(y - \frac{h}{2}\right)^2 + \frac{h^2}{4}} dy. \end{aligned} \quad (2.31)$$

This is identical in form to Equation (2.21), and so the result is

$$U_k = \sqrt{2}U_0 \sqrt{\frac{4\Delta U}{h^2}} \frac{h^2}{8} \pi = \frac{\pi h}{2\sqrt{2}} \sqrt{\Delta U U_0}, \quad (2.32)$$

which is half the prefactor of Equation (2.23).

Hence, we have that for the LT model, under a high stress and lower temperature regime, the activation enthalpy for kink-pair nucleation is given by

$$\Delta H = 2U_k \left(1 - \frac{\tau}{\tau_p}\right)^2, \quad (2.33)$$

where $U_k = \frac{\pi h}{2\sqrt{2}} \sqrt{\Delta U U_0}$ is the energy of an isolated kink.

Testing The Model

Predictions for the Peierls stress and kink-pair energy ($2U_k$) in α -Fe have been obtained using three of the potentials shown in Figure 2.2, which are shown in their functional form in Table 2.1 along with their associated expressions for the kink-pair energy (derived using Equation (2.30)) and Peierls stress. These predictions are shown in Table 2.2 along with experimental values and predictions that used ES calculations based on the density functional theory (DFT). The predictions based on the sinusoidal potential are closest to the reference values.

The discrepancy between the experimental values for τ_p and the others in Table 2.2 is a common feature found in the literature, which is attributed to not taking into account zero-point energy vibrations and non-glide effects such as interactions with other dislocations^[56,57].

The parameters used for the predictions based on the model potentials came from

Table 2.1: Showing the functional form of three of the potentials shown in Figure 2.2, along with their associated kink energies, calculated using Equation (2.30), and their Peierls stresses, found from their maximum gradient^[46].

Potential $U(y)$	Kink-Pair Energy $2U_k$	Peierls Stress τ_p
Parabolic $U_0 + 4\Delta U \frac{y}{h} \left(1 - \frac{y}{h}\right)$	$\frac{\pi}{2^{1/2}} h (\Delta U U_0)^{1/2}$	$4 \frac{\Delta U}{hb}$
Sinusoidal $U_0 + \frac{\Delta U}{2} \left(1 - \cos \frac{2\pi y}{h}\right)$	$\frac{2^{5/2}}{\pi} h (\Delta U U_0)^{1/2}$	$\pi \frac{\Delta U}{hb}$
Eshelby $U_0 + 16\Delta U \left(\frac{y}{h}\right)^2 \left(1 - \frac{y}{h}\right)^2$	$0.943h (\Delta U U_0)^{1/2}$	$3.08 \frac{\Delta U}{hb}$

Table 2.2: Showing values for the kink-pair energy $2U_k$ and the Peierls stress τ_p in α -Fe, calculated using the three potentials and the formulae in Table 2.1. The parameters used were $b = 2.49 \text{ \AA}^{[11]}$, $h = 2.31 \text{ \AA}^{[11]}$, $\Delta U = 0.035 \text{ eV b}^{-1}$ ^[32] and $U_0 = 3.57 \text{ eV \AA}^{-1}$ ^[32,50,51]

	Parabolic	Sinusoidal	Eshelby	DFT	Experimental
$2U_k/(\text{eV})$	1.15	0.93	0.98	0.73–0.91 ^[32,50,51]	0.60–0.91 ^[52–54]
$\tau_p/(\text{MPa})$	1572	1235	1210	1000–1450 ^[32,50,51]	370–395 ^[54,55]

four sources: the value for the Peierls barrier of $\Delta U = 0.035 \text{ eV b}^{-1}$ (i.e. eV per Burgers vector) was obtained from Itakura *et al*^[32]; those for the Burgers vector and distance between Peierls valleys, respectively $b = 2.49 \text{ \AA}$ and $h = 2.31 \text{ \AA}^{[11]}$, from Katzarov *et al*^[11]; and that for the LT/dislocation ground state energy of $U_0 = 3.57 \text{ eV \AA}^{-1}$ was the arithmetic mean of those from three of the sources^[32,50,51]. The values for ΔU and U_0 from the reference sources were calculated using DFT. Those for U_0 were calculated using three different DFT codes (VASP, SIESTA and PWSCF, respectively 3.08 eV \AA^{-1} , 4.1 eV \AA^{-1} and 3.52 eV \AA^{-1}), and so the average was taken. The dislocation LT was calculated similarly in all three reference sources using a discretized form of Equation (2.6) so that results from atomic-scale simulations, where in-row atomic displacements are constrained to reproduce the first stage of the formation of a kink-pair, could be utilised. The DFT values for the kink-pair energy in Table 2.2 were calculated in a similar way.

It was found by Dezerald *et al*^[51] that values for the LT computed using anisotropic elasticity, which were corrected for dislocation core energy contributions, were 35% less than the DFT values. They noted that this discrepancy illustrates “the limitation of applying elasticity to highly localized processes like kink-pair formation, which

involves dislocation segments with a length comparable to the core radius.” They also noted that the difference between isotropic and anisotropic elastic LT values was much smaller than the difference between the elastic and DFT LT values, confirming that “the discrepancy does not stem from anisotropy, but that it is related to the atomistic nature of the process.”

2.2.2 Elastic Interaction Model

In the low stress and higher temperature regime that applies for this model, thermal fluctuations are large enough to allow fully developed kink-pairs (i.e. the leading part of the kink-pair nucleus reaches the next potential valley) to form on the dislocation. The kinks interact elastically with each other, and in the saddle configuration this attractive elastic interaction (EI) is just balanced by the applied stress, which tends to pull them apart. The saddle configuration is shown in Figure 2.1(a), where it can be seen that the kink separation L is greater than the kink width w in this regime. The enthalpy H for a kink-pair in this regime consists of the energy of two isolated kinks $2U_k$, their interaction energy I_{kk} and the work done by the applied stress τ :

$$H = 2U_k + I_{kk} - \tau bhL, \quad (2.34)$$

where h is the distance between potential valleys (note that this is λ in Figure 2.1). The interaction energy I_{kk} is given by^[46]

$$I_{kk} = -\frac{\mu b^2 h^2}{8\pi L}, \quad (2.35)$$

where μ is the elastic shear modulus, to find the activation energy, H must be maximised with respect to L :

$$L^* = \left(\frac{\mu bh}{8\pi\tau} \right)^{1/2}; \quad (2.36)$$

i.e. L^* is the critical separation of the kinks for which H is at a maximum, which defines the saddle-point configuration. The activation energy is therefore given by

$$\Delta H = 2U_k \left[1 - \left(\frac{\tau}{\tau^*} \right)^{1/2} \right], \quad \text{where} \quad \tau^* = 2U_k \left[\frac{2\pi}{h^3 b^3 \mu} \right]^{1/2}. \quad (2.37)$$

2.2.3 Model Validity

Equation (2.36) shows that as the applied stress τ increases, the critical separation of the kinks L^* decreases; when this separation approaches the kink width w and below, the validity of the EI model becomes questionable. This is because the elastic strain fields of the two kinks begin to overlap more than can be handled by linear elasticity (i.e. Hooke's law becomes invalid). A physical picture using the Peierls potential is then required to describe the kink-antikink interaction; however, at this stage, where $L \sim w$, the line tension model is not appropriate either as there is no "bulge" ($\frac{dy}{dx}$ is imaginary).

Caillard and Martin^[46] have estimated the stress interval where neither of the models apply. They use the abrupt potential, which is shown in Figure 2.2, to do so, as the kink width is well defined for this potential:

$$w = h \left(\frac{U_0}{2\Delta U} \right)^{1/2}, \quad (2.38)$$

and equating this with Equation (2.36) leads to

$$\tau_{\max}^{(\text{EI})} = \frac{\mu b}{4\pi h} \frac{\Delta U}{U_0}, \quad (2.39)$$

which gives an estimate of the maximum stress allowed in elastic interaction (EI) model. For an estimate of the minimum allowed stress in the line tension (LT) model, he uses the constraint that the critical bulge must not extend more than the distance between Peierls valleys; i.e. $y_s \leq h$, which leads to

$$\tau_{\min}^{(\text{LT})} = \frac{\Delta U}{hb}. \quad (2.40)$$

It may be helpful to express these as a fraction of the Peierls stress. As the abrupt potential has an infinite Peierls stress, that of the parabolic potential will be used

instead, as it shares a similar quality in that it keeps the dislocation trapped in the Peierls valley (until the Peierls stress is met). This gives

$$\frac{\tau_{\max}^{(\text{EI})}}{\tau_p} = \frac{\mu b^2}{16\pi U_0} \approx \frac{1}{16\pi} \quad \text{and} \quad \frac{\tau_{\min}^{(\text{LT})}}{\tau_p} = \frac{1}{4}. \quad (2.41)$$

where double the standard isotropic elasticity estimate for the LT ($\approx \mu b^2/2$) has been used to take into account the findings of Dezerald *et al*^[51].

Caillard has more recently shown^[37] for α -Fe at room temperature that the EI model is not consistent with a stress of 37 MPa. This was done by comparing an experimentally determined activation area with that predicted by the EI model; i.e. from Equation (2.37)

$$\Delta A = -\frac{1}{b} \left(\frac{\partial \Delta H}{\partial \tau} \right)_T = \left(\frac{h^3 b \mu}{8\pi \tau} \right)^{1/2} = hL^* \quad (2.42)$$

Using Equation (2.41) and $\tau_p \approx 400$ MPa, we obtain $\tau_{\max}^{(\text{EI})} \approx 8$ MPa, which is, considering the two unphysical potentials that were used to derive this estimate, surprisingly consistent with the experimental finding that $\tau_{\max}^{(\text{EI})} < 37$ MPa. So, we may take Equations (2.41) as providing at least loose estimates of $\tau_{\max}^{(\text{EI})}$ and $\tau_{\min}^{(\text{LT})}$.

2.2.4 Kocks' Law

The simple LT model described above has been shown to be consistent with experiment using the anti-parabolic potential by Argon^[15] and the reference data in Table 2.2 is most closely described by use of the model with a sinusoidal potential. Also, for high stresses close to τ_p , a functional form for the activation energy that is derived using the Eshelby potential is often used to fit experimental data^[33,46,54,58]:

$$\Delta H = \frac{12}{5} U_k \left[\frac{2}{3} \left(1 - \frac{\tau}{\tau_p} \right) \right]^{5/4}. \quad (2.43)$$

The form of Equations (2.33), (2.37) and (2.43) indicate that, in general, ΔH can be described by an equation of the form

$$\Delta H = \Delta H_0 \left[1 - \left(\frac{\tau}{\tau_p} \right)^p \right]^q, \quad (2.44)$$

where p and q are adjustable parameters and $\Delta H_0 = 2U_k$ is the energy of two isolated kinks (i.e. under zero applied stress). This equation is widely referred to as “Kocks law” after Kocks *et al*^[17] who proposed it.

Given the inadequacy of the EI and LT models to accurately describe an intermediate stress regime, in addition to the fact that the Peierls potential is modified by the applied stress tensor^[25,26], the phenomenological generalisation of Kocks’ law is commonly used to describe the stress dependence of the activation energy. It is fitted to atomistic data through the adjustable parameters p and q , which may take values of $0 < p \leq 1$ and $1 \leq q \leq 2$.

2.3 The Frequency Prefactor

As stated earlier, the frequency prefactor for the kMC event rates f could be estimated using HTST:

$$f = \frac{\prod_{i=1}^{3N} \nu_i}{\prod_{i=1}^{3N-1} \nu'_i}, \quad (2.45)$$

where N is the number of atoms in the system and the ν_i and ν'_i are the vibrational frequencies of the system in the ground state and at the saddle point, respectively (one of the frequencies at the saddle point is imaginary corresponding to a negative eigenvalue of the Hessian matrix). However, this is computationally expensive for large systems. An approximation to this (approximation) would be to only consider L/b degrees of freedom, where L is the length of the dislocation, and solve the string differential equation for the dislocation in both states, i.e. Equation (2.7) with an inertial term, to obtain the vibrational frequencies^[59]. In practice, however, simpler estimation methods are used, some of which are described in the following. Also, since only kink-pair nucleation rates need to be considered in this work (as will be explained later) the prefactor will be designated f_{kn} from now on.

The simplest form of estimation has been to use the Debye frequency ν_D ^[6,60–63], which corresponds to uncorrelated atomic motion, of the element being modelled. This is an overestimate, though, as a dislocation through its line tension correlates the motion of its constituent atoms, and so the atomic motions should have longer

wavelengths. A better estimate given in Caillard and Martin^[46] is

$$f_{\text{kn}} = \frac{b}{l} \nu_{\text{D}}, \quad (2.46)$$

where l is the length of the dislocation segment in question. A slightly more complicated estimate, which is commonly used^[12,19,21], is given by the fundamental mode of the Granato-Lücke vibrating string model, which is described in Anderson, Hirth and Lothe^[2],

$$f_{\text{kn}} = \frac{\pi}{l} \sqrt{\frac{\mu}{\rho}}, \quad (2.47)$$

where μ and ρ are, respectively, the shear modulus and the mass density of the material in question ($\sqrt{\frac{\mu}{\rho}}$ is the shear wave velocity). This is similar to the fundamental harmonic f of a vibrating string:

$$f = \frac{1}{2l} \sqrt{\frac{T_L}{(m/l)}}, \quad (2.48)$$

where T_L is the line tension and m is the mass.

Finally, a form of estimation that can be inferred from Taylor^[64], is to assume that a dislocation segment's velocity obeys a Boltzmann distribution as it passes through the saddle point during kink-pair nucleation, then

$$f_{\text{kn}} = \frac{1}{y_s} \left(\frac{k_B T}{2\pi m} \right)^{1/2}, \quad (2.49)$$

where y_s is the distance of the saddle point from the ground state position.

The last two methods of estimation require that the dislocation mass per unit length is known. For a screw dislocation, this is obtained from^[15,17,65]

$$U(v) = \frac{U_0}{\sqrt{1 - (v/c_s)^2}} \simeq U_0 + \frac{1}{2} \left(\frac{U_0}{c_s^2} \right) v^2 + \dots \quad (v/c_s \ll 1); \quad (2.50)$$

i.e. a dislocation's line energy per unit length as a function of its velocity v is the dislocation line energy per unit length in the ground state $U_0 \simeq T_L$ scaled by a "Lorentz" factor, where $c_s = \sqrt{\frac{\mu}{\rho}}$ is the shear wave velocity. Assuming the standard

Table 2.3: Showing the formulae and calculated values, using α -Fe parameters, of the estimates for f_{kn} discussed in this section. The parameters used were $\theta_{\text{D}} = 470\text{K}$ (note that h here is Planck's constant), $b = 2.49 \text{ \AA}$, $l = 30b$, the room temperature shear modulus^[66] $\mu = 71 \text{ GPa}$, $\rho = 7874 \text{ kg m}^{-3}$, $y_s = 2.31 \text{ \AA}$ (i.e. the distance between Peierls valleys), $T = 300 \text{ K}$ and $U_0 \simeq T_L = 3.57 \text{ eV \AA}^{-1}$.

	Debye	Caillard	G-L String	String	Taylor
Formula	$\nu_{\text{D}} = \frac{k_B \theta_{\text{D}}}{h}$	$\frac{b}{l} \nu_{\text{D}}$	$\frac{\pi}{l} \sqrt{\frac{\mu}{\rho}}$	$\frac{1}{2l} \sqrt{\frac{\mu}{\rho}}$	$\frac{1}{y_s} \left(\frac{k_B T}{2\pi l U_0} \frac{\mu}{\rho} \right)^{1/2}$
$f_{\text{kn}}/10^{11} \text{ s}^{-1}$	97.9	3.26	12.7	2.01	0.511

kinetic energy formula, the mass is then given by

$$m = l \frac{U_0}{c_s^2}. \quad (2.51)$$

Using these formula with α -Fe parameters, values for f_{kn} ranging from 10^{10} to 10^{13} s^{-1} are obtained. These calculated values are shown in Table 2.3 along with their respective formulae after substituting for m .

Given the spread of values for these methods of estimation it would seem that the best approach is to fit the prefactor to experimental data as was done by Katzarov *et al*^[11], and this is the method adopted in this work.

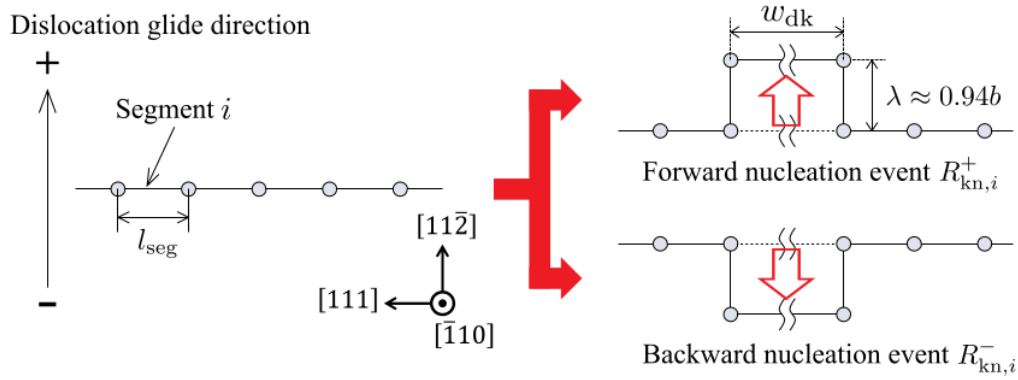
Chapter 3

The Kinetic Monte Carlo Model

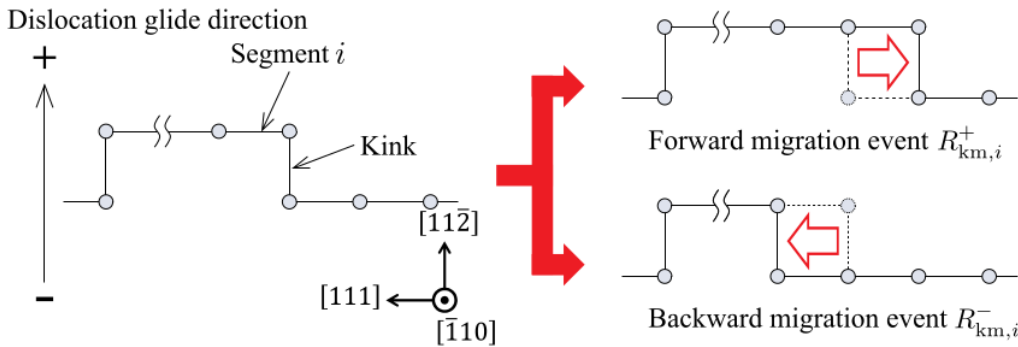
Dislocation kMC models are based on a grid structure to replicate the form of a lattice, with the minimum spacing between points in one direction being the magnitude of the Burgers vector of the dislocation b and the spacing in the other direction(s) being the unit kink-height h ; i.e. the spacing between Peierls valleys. The elementary events of kink-pair nucleation and migration that these dislocation simulations progress through are illustrated in Figure 3.1 for a $\frac{1}{2}\langle 111 \rangle\{110\}$ screw. Kink annihilation is a special case of either of the former, occurring when opposite kinks meet on the same plane. Activation energies for these events depend on the local stress conditions, which can be determined through the use of isotropic elasticity to calculate energy interaction terms between dislocation segments or the local stress can be calculated directly.

3.1 Previous Studies

The earliest dislocation kMC model was introduced by Lin and Chrzan^[19]. They studied the effect of finite simulation cell size on dislocation velocity and showed that for low applied stresses dislocation velocity decreased with dislocation length. At low applied stresses kink-pairs are more unstable and can annihilate immediately after nucleation. The free surfaces in their simulations stabilised kink-pairs that nucleated near to them, acting as kink sources; however as dislocation length increased and the ratio of surface to bulk nucleation sites decreased, velocity was seen to decrease. At high stresses where kink-pairs are more stable, dislocation velocity was seen to



(a) Double-kink nucleation.



(b) Kink migration.

Figure 3.1: Illustrating the kMC events that describe screw dislocation glide in bcc metals^[13].

increase with length, due to more nucleation sites being available. They avoided the bottleneck of kMC simulations where almost all embryonic kink-pairs of separation b annihilate immediately after nucleation by choosing the kink-pair separation to be $20b$. Cai *et al*^[60] improved upon this by using a survival probability method to calculate the rate at which kink-pairs of a prescribed separation form from an embryonic state of separation b in their simulations of a dissociated screw dislocation in silicon. They also incorporated atomistic data regarding energy barriers and used periodic boundary conditions to avoid surface effects. The former models were two-dimensional, a three dimensional model was later introduced by Cai *et al*^[61], which simulated a screw dislocation in a bcc metal. Kink-pairs could nucleate on three types of $\{110\}$ planes as shown in Figure 3.2 where the planes intersect a $\langle 111 \rangle$ direction along which a dislocation is mostly aligned. Figure 3.3 illustrates possible kink intersections permitted in this model. When opposite kinks that have formed on different planes intercept, they cannot annihilate and are constrained to move together due to the forces due to the external stress acting on them in opposite

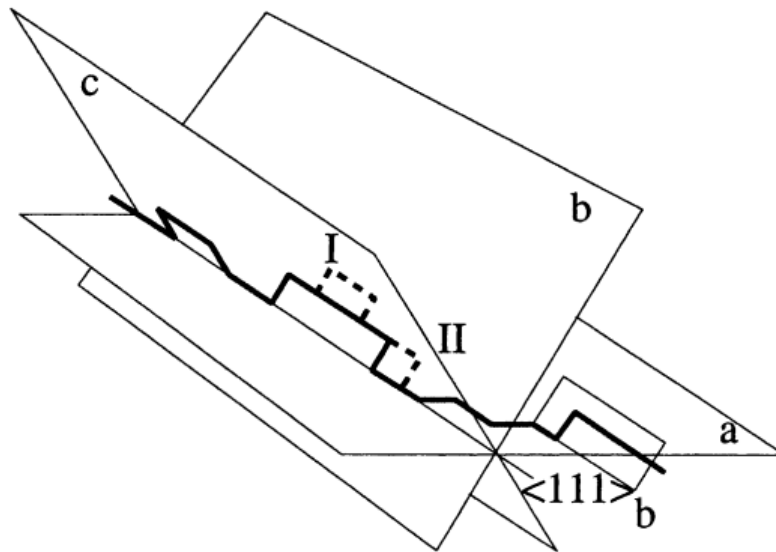


Figure 3.2: Schematic representation of a dislocation in a bcc metal in the kMC model. The dislocation line is mostly aligned along a $\langle 111 \rangle$ direction. Kink-pairs can nucleate on any of three types of $\{110\}$ plane a , b and c . A kink-pair nucleation event is shown at position I and a kink migration event is shown at position II, both in dashed lines^[61].

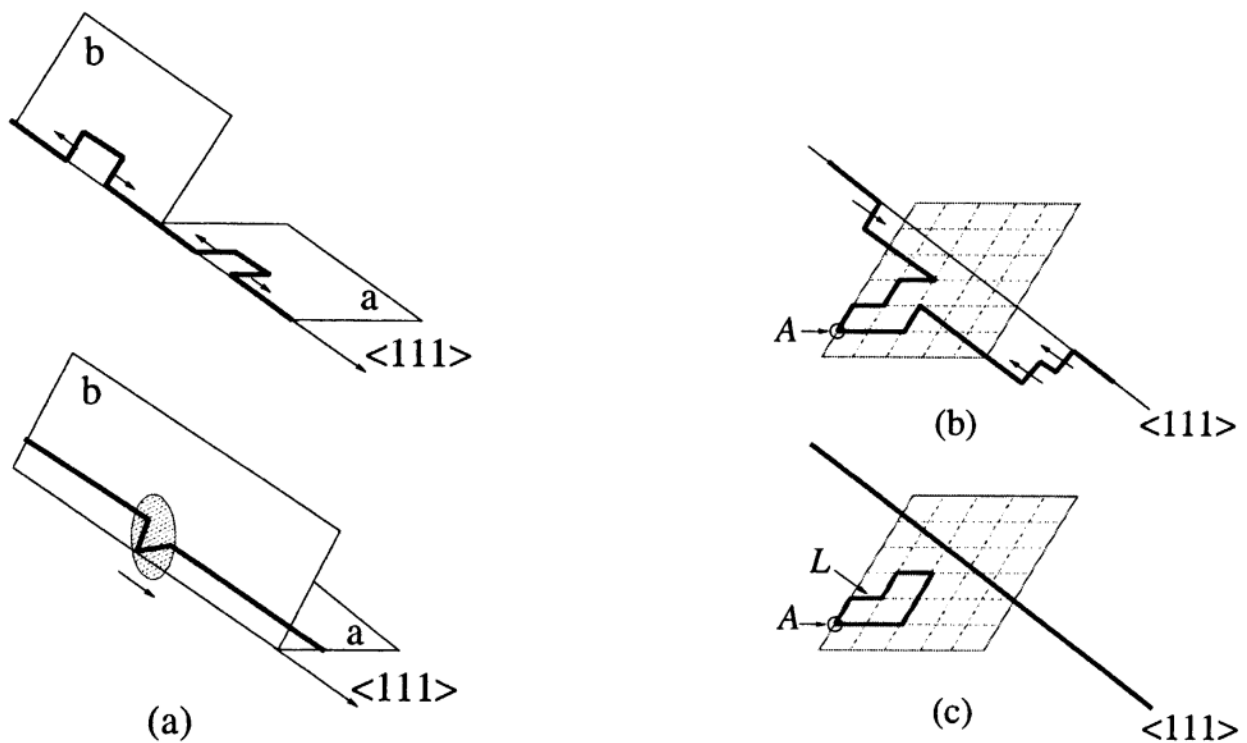


Figure 3.3: Schematic representation of the formation of (a) two kinks forming a cross-kink, (b) more kinks joining the cross-kink in a *pile-up*, and (c) debris loop L formation with the primary dislocation breaking away from the self-pinning point A .^[61]

directions (sect. 1.3.2). A *cross-kink* is thus formed (Figure 3.3(a)), which moves relatively slowly compared with solo kinks and may even stop moving altogether, and so acts as a pinning point for the dislocation. More kinks can *pile-up* at the initial pinning point (Figure 3.3(b)) and the dislocation may be able to break free if a certain combination of kinks pile-up forming a *debris loop* in the process (Figure 3.3(c)). The presence of these pinning points/pile-ups mean that many kink-pairs will annihilate without contributing to overall dislocation motion, and dislocation velocity will eventually stop increasing with length at high stresses, even slowing down, in contrast to what Lin and Chrzan^[19] demonstrated. In the same model, Cai *et al*^[61] used a line tension model to calculate the kink-pair nucleation enthalpy as a function of applied stress, using as input atomistic data for the nucleation energy barrier in the absence of external stress (cf. ΔH_0 , Equation (2.44)). They also dealt with kink migration events differently in this model, as the energy barrier for kink migration in bcc metals is negligible, and so it's not a thermally activated (rare) event. It's limited by a phonon drag mechanism and, in this model, it was assumed to occur at a constant speed v_k , which was calculated for each kink according to the local stress conditions every kMC step:

$$v_k = \frac{\tau_{\text{eff}} b}{B}, \quad (3.1)$$

where τ_{eff} is the effective local stress field (resolved in the glide plane) composed of the applied stress field and stress field contributions from other dislocation segments, and B is the drag coefficient.

Dislocation solute interactions were introduced by Deo *et al*^[20] in their kMC model of a $\frac{1}{2}\langle 111 \rangle \{110\}$ screw in bcc Tantalum. The dislocation motion was planar with solute atoms distributed in three-dimensions. Simulations were performed to determine dislocation velocity as a function of stress, temperature and solute concentration. They accounted for the presence of solute atoms with respect to kink-pair nucleation by adding an energy parameter to the nucleation enthalpy when the nucleation site was at a solute position. The effect of solute atoms on kink migration was dealt with in two ways. For solute atoms that were further than a prescribed distance from a kink, they were accounted for elastically by adding a contribution to the local stress field that the kink experienced and the kink would

migrate according to Equation (3.1). Solute atoms that were closer to kinks were accounted for by making the kink migration a thermally activated event; i.e. the solute atoms constituted an energy barrier to kink motion – a solute-dislocation core interaction – and the velocity with which a kink bypassed a solute along its path was described by an Arrhenius type equation with a stress and temperature dependent prefactor. They found that solute atoms served to reduce the dislocation velocity and that the dominant solute-dislocation interaction was the short-range core interaction rather than the long-range elastic one due to the stress fields. They noted that the accuracy of their simulations was limited by uncertainty in atomistic parameters such as single kink energy, solute–dislocation core interaction energies, etc.

Building upon the previous work of other authors, Stukowski *et al*^[21] entirely parameterised their kMC model for a screw dislocation in bcc tungsten, which allowed for cross-slip following Cai *et al*^[61], with atomistic calculations based on an EAM[†] potential, fitting their kink-pair nucleation enthalpy data to a Kocks' law (Equation (2.44)) and incorporating the variation of CRSS with pure shear stresses applied on different MRSS planes; i.e. non-Schmid effects. Although they didn't include non-glide stresses in their model, they still showed that the non-Schmid effects that they did include had a strong influence on the dislocation velocity.

More recently, Katzarov *et al*^[11], advancing the model by Deo *et al*^[20], studied the effect of hydrogen, an interstitial solute, on screw dislocation velocity in α -Fe. They incorporated recently available, more accurate atomistic data based on DFT calculations, which included kink-pair nucleation and kink migration energies, both as a function of hydrogen concentration. These data parameterised a line tension model such that kink-pair nucleation energy as a function of applied stress could be obtained. In contrast with the model by Deo *et al*^[20], their model allowed for cross-slip of the dislocation as in the model by Cai *et al*^[61]. They were able to make quantitative estimates regarding the ratio of dislocation velocities obtained from simulations that included hydrogen to the velocities obtained from simulations for pure iron, after identifying regimes of applied shear stress, temperature and

[†] An EAM or *embedded atom model* describes approximately the energy between atoms; i.e. it's an interatomic potential. Contrast with DFT which uses full electronic structure calculations, but which cannot, however, model as large a system size as possible with an interatomic potential.

hydrogen concentration within which the dislocation velocity differed from that in pure iron.

A final model that will be considered is that of Shinzato *et al*^[13]. They studied the effect of the substitutional solute of silicon on screw dislocation velocity in α -Fe parameterising their model on atomistic calculations based on interatomic potentials. Their model didn't allow for cross-slip of the dislocation, however, and they noted that, although their results agreed qualitatively with experimental observations (e.g. dislocation velocity increased at low temperatures in the presence of silicon compared with that in pure iron, i.e. *solid solution softening*, and the reverse at high temperatures, i.e. *solid solution hardening*), there was a quantitative discrepancy between their results and experiment, which they identified with the fact that their simulations were two-dimensional. This demonstrating the importance of accounting for three-dimensional kink behaviour such as cross-kink formation as described in the model by Cai *et al*^[61].

3.2 Implementation

The model presented in this work follows that of Cai *et al*^[61] and is described as follows. The dislocation has a maximum length of $L_D = 1000b$ consisting of pure screw segments of length $b = \frac{\sqrt{3}}{2}a_0$, where a_0 is the lattice parameter of α -Fe, oriented along the $\frac{1}{2}[111]$ direction, and kinks of length $h = \frac{\sqrt{6}}{3}a_0$ oriented along any one of six $\frac{1}{3}\langle 112 \rangle$ directions. Periodic boundary conditions are applied along the $\frac{1}{2}[111]$ direction such that kinks exiting the dislocation at one end will reenter from the other. The kinks are represented by pure edge segments, i.e. they have zero width (e.g. Figure 2.1(a) with $w = 0$ or the kinks in Figure 3.1), which is an appropriate approximation when the kink-pair separation L is greater than the kink width w ^[11,63]. This has been shown to be the case by Itakura *et al*^[32] who showed that $w \approx 10b$ and $L \approx 20b$ with their line tension model. The model presented here doesn't distinguish between left and right kinks nor does it allow for the climb of edge segments.

Figure 4.1 shows glide planes of the $[111]$ zone: the six $\frac{1}{3}\langle 112 \rangle$ directions are contained in the three $\{110\}$ glide planes of the zone; the x -, y - and z -directions are

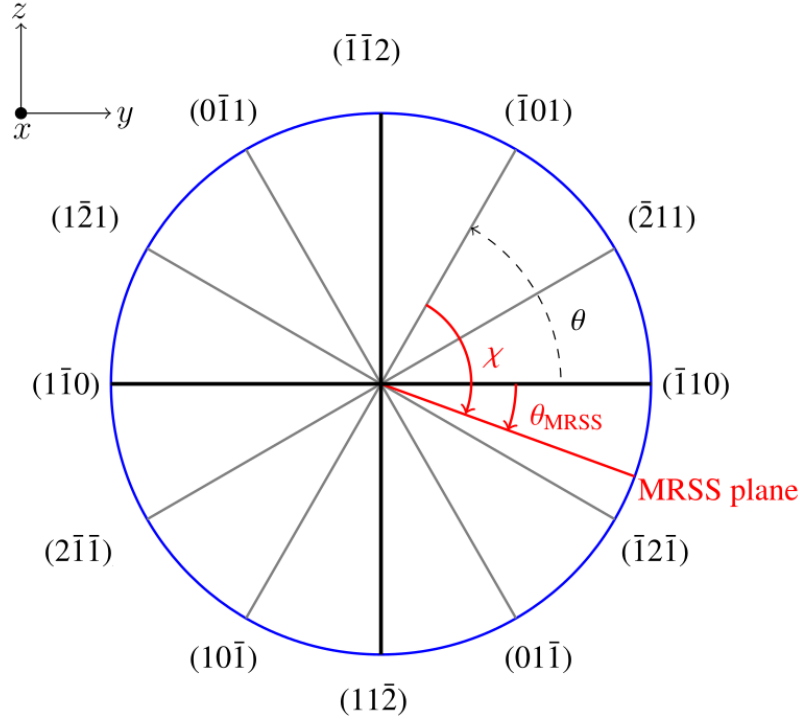


Figure 3.4: “Schematic view of the glide planes of the $[111]$ zone. A generic MRSS plane is labeled in red, while, by way of example, the $(\bar{1}01)$ is the glide plane.^[21]”

oriented along the $[111]$, $[11\bar{2}]$ and $[\bar{1}10]$ directions, respectively; the $\pm(\bar{1}10)$, $\pm(\bar{1}01)$ and $\pm(0\bar{1}1)$ planes, respectively, correspond to the ‘a’, ‘b’ and ‘c’ type planes referred to in Figure 3.2; the angle θ is measured in an anti-clockwise sense from the $(\bar{1}10)$ plane; the angle θ_{MRSS} is measured from the $(\bar{1}10)$ plane to the MRSS plane; and the angle χ is measured from the active glide plane to the MRSS plane.

As non-Schmid effects are not considered in this model, only two components of the applied stress tensor $\boldsymbol{\tau}$ need to be specified for a kMC run. From the Peach-Koehler formula (1.6), for a dislocation with $\mathbf{b} = b\mathbf{e}_x$ and $\boldsymbol{\xi} = \mathbf{e}_x$, we have

$$\mathbf{f} = b(\tau_{xz}\mathbf{e}_y - \tau_{xy}\mathbf{e}_z), \quad (3.2)$$

such that the stress component $\tau_{xz} > 0$ induces glide in the $+y$ -direction along ‘a’ type planes and the component $\tau_{xy} < 0$ leads to a force in the $+z$ -direction, and so induces cross-slip on to ‘b’ and ‘c’ type planes. The MRSS plane is thus specified by

$$\theta_{\text{MRSS}} = \tan^{-1}\left(-\frac{\tau_{xy}}{\tau_{xz}}\right), \quad (3.3)$$

and the resolved shear stress (RSS) in the glide plane for the i^{th} screw segment is given by

$$\begin{aligned}\tau_i(\theta) &= \mathbf{e}_x \cdot \boldsymbol{\tau}_i^{\text{eff}} \cdot \hat{\mathbf{n}} = \mathbf{e}_x \cdot \left(\boldsymbol{\tau} + \sum_j \tau_{ij}(r_{ij}) \right) \cdot (-\mathbf{e}_y \sin \theta + \mathbf{e}_z \cos \theta) \\ &= -\tau_{i,xy}^{\text{eff}} \sin \theta + \tau_{i,xz}^{\text{eff}} \cos \theta,\end{aligned}\quad (3.4)$$

where \mathbf{e}_x is the slip direction, $\hat{\mathbf{n}}$ is the glide plane normal and $\boldsymbol{\tau}_i^{\text{eff}}$ is the effective local stress that the segment experiences due to contributions from the applied stress field and the stress fields of all other j segments. The distance between the i^{th} and j^{th} segments is r_{ij} , with the stress field of the j^{th} segment being evaluated at the i^{th} segment's midpoint. The internal stress field contributions are computed using non-singular isotropic[†] elasticity theory^[69]. Both the kink-pair nucleation rate on each screw segment and the the kink velocity depend on the effective local stress field, with the velocity of each kink \mathbf{v}_{k_i} being proportional to its driving force:

$$\begin{aligned}\mathbf{v}_{k_i} &= \frac{1}{B} (\mathbf{b} \cdot \boldsymbol{\tau}_i^{\text{eff}}) \times \boldsymbol{\xi}_i = \frac{b}{B} (\tau_{i,xy}^{\text{eff}} \mathbf{e}_y + \tau_{i,xz}^{\text{eff}} \mathbf{e}_z) \times (\mathbf{e}_y \cos \theta + \mathbf{e}_z \sin \theta) \\ &= \frac{b}{B} (\tau_{i,xy}^{\text{eff}} \sin \theta - \tau_{i,xz}^{\text{eff}} \cos \theta) \mathbf{e}_x,\end{aligned}\quad (3.5)$$

where $B = (2.7 + 0.008T) \times 10^{-5}$ Pa.s^[70]. There are six kink-pair nucleation rates for each screw segment, which correspond to forwards and backwards nucleation on each type of plane:

$$J_{\theta,i}^{+/-} = f_{\text{kn}} \exp\left(-\frac{\Delta H(\tau_i(\theta))}{k_B T}\right),\quad (3.6)$$

and writing $\Delta H(\tau_i(\theta))$ in a Kocks' law format, we have

$$\Delta H(\tau_i(\theta)) = \Delta H_0 \left[1 - \left(\frac{\tau_i(\theta)}{\tau_p} \right)^p \right]^q \quad \text{for } \theta = 0, \frac{\pi}{3}, -\frac{\pi}{3},\quad (3.7)$$

which corresponds to forwards nucleation on 'a', 'b' and 'c' planes, respectively, and

$$\Delta H(\tau_i(\theta)) = \Delta H_0 \left\{ 2 - \left[1 - \left(\frac{\tau_i(\theta)}{\tau_p} \right)^p \right]^q \right\} \quad \text{for } \theta = \pi, -\frac{2\pi}{3}, \frac{2\pi}{3},\quad (3.8)$$

[†] Although α -Fe is in general an anisotropic elastic material, the shear modulus in the [111] zone is isotropic^[67,68], and so this mitigates the effect of using an isotropic theory.

which corresponds to backwards nucleation on ‘a’, ‘b’ and ‘c’ planes, respectively.

A simulation then proceeds according to the following algorithm.

1. At the beginning of each kMC step, stress is calculated along the entire dislocation line, such that the kink velocities and the kink-pair nucleation rates on each screw segment can be determined using Equations (3.5) and (3.6), respectively.
2. Assuming that the kinks move with constant velocity, a migration time t_{mig} is computed, which is the time that the fastest kink takes to migrate a prescribed distance x_{mig} , or before any kink reactions occur (i.e. kink annihilation, cross-kink formation or debris loop formation).
3. A nucleation time t_{nuc} is randomly selected from the exponential distribution, according to the total dislocation line nucleation rate (cf. Section 1.2).
4. If $t_{\text{mig}} < t_{\text{nuc}}$, then each kink is migrated a distance $|\mathbf{v}_{k_i}| \times t_{\text{mig}}$, any kink reactions are carried out and the simulation time is incremented by t_{mig} . Otherwise, each kink is migrated a distance $|\mathbf{v}_{k_i}| \times t_{\text{nuc}}$ followed by kink-pair nucleation on a screw segment, the segment chosen according to the standard kMC algorithm (Section 1.2). Time is incremented by t_{nuc} and the algorithm returns to step 1.

Two further points to note are that cross-kink/kink pile-up velocity is computed as the arithmetic mean of the velocities of the constituent kinks according to τ_i^{eff} each kMC step, and that upon debris loop formation[†] the pile-up is reduced in size and the dislocation line is reduced in length according to the size of the debris loop.

3.3 Dislocation Velocity

Under high stresses, kink-pair nucleation time is the rate-limiting step in dislocation motion, and according to Anderson, Hirth and Lothe^[2], the velocity v of a dislocation normal to itself moving under stress by the kink-pair mechanism is given by

$$v = hXJ, \tag{3.9}$$

[†]In pile-ups of three or more kinks, a simple algorithm detects when a kink start point equals the end point of another kink.

where J is the kink-pair nucleation rate per unit length of the dislocation and X is the average distance along the dislocation swept out by one kink pair before it annihilates with the kinks from other pairs, which assumes motion on a single plane. When the dynamics is governed by the existence of a single kink-pair on the dislocation line at any one time, X is simply the length of the dislocation L_D , the distance at which the kink-pair will annihilate with its periodic image, and JL_D is the total nucleation rate of the perfectly straight dislocation. Kink migration is assumed to be instantaneous[†] in this case. For higher average concentrations of kink-pairs on the dislocation line, a suitable measure for X is the geometric average

$$X = \frac{L_D c_{kp}^{-1}}{L_D + c_{kp}^{-1}}, \quad (3.10)$$

where c_{kp} is the average concentration of kink-pairs. A geometric average is appropriate as L_D and c_{kp} are competing quantities. This is because v will increase with L_D due to more nucleation sites becoming available; however, as c_{kp} increases the distance between kink-pairs becomes important also, as the kink-pairs will annihilate before traversing the length of the dislocation, which serves to reduce v compared with the single kink-pair dynamic. For example, for $c_{kp} > 1$ the kMC clock is incremented by nucleation time more than once, but the dislocation will still only advance by h in that time. Although the average kink-pair concentration can readily be obtained from simulations, it can also be determined from the condition of steady-state motion of the dislocation. This requires that the migration time between annihilation events equals the average time required for a nucleation event over the average length of a growing kink-pair^[2,71]:

$$\frac{(c_{kp}^{-1})/2}{v_k} = \frac{1}{J(c_{kp}^{-1})/2} \Rightarrow c_{kp}^{-1} = 2\sqrt{\frac{v_k}{J}}, \quad (3.11)$$

where v_k is the average kink velocity so that

$$v = 2h\sqrt{Jv_k} \frac{L_D}{L_D + c_{kp}^{-1}}, \quad (3.12)$$

where J would be the average simulation nucleation rate in this case.

[†]Simulations have shown kink migration times to be up to 10^{18} smaller than nucleation times

Chapter 4

Results and Discussion

In order to determine the viability of the kMC model, a number of tests have been performed. These tests and their results will now be described in the following sections.

4.1 Comparison with Reference Data I

The results of the attempt to replicate the pure iron velocity data from Katzarov *et al*^[11] will be presented in this section.

The parameters used are listed in Table 4.1. Where possible they were obtained from the reference; however, with two exceptions: the non-singular elasticity theory core cut-off parameter r_c and the frequency prefactor f_{kn} . The cut-off parameter was calibrated such that the excess energy of a dislocation under zero applied stress with a kink-pair of separation of $L = 30b$ equalled 0.69eV, as stated in the reference. The value of the cut-off parameter was determined to be $r_c = 0.305b$, whereas the reference value is $r_c = 0.48b$: this difference most likely being the result of using different values for the elastic shear modulus μ and Poisson's ratio ν , which were not given in the reference. The reference frequency prefactor was calibrated such that the dislocation velocity matched an experimentally estimated value^[37]. The same method was used in this work; however, calibrating the prefactor such that the dislocation velocity matched the reference value at a temperature of 300 K with an applied stress of 50 MPa. This still led to a good match with the experimentally estimated velocity at $T = 300$ K and $\tau = 33$ MPa. The prefactor came out to be

Table 4.1: List of parameters and functional dependencies used in the kMC model.

Parameter	Value or Function	Units
a_0	2.87	Å
b	$a_0\sqrt{3}/2$	Å
h	2.31	Å
μ	71	GPa
ν	0.28	–
r_c	0.305	b
x_{mig}	5	b
L	30	b
L_D	1000	b
\mathbf{v}_{k_i}	$B^{-1}(\mathbf{b} \cdot \boldsymbol{\tau}_i^{\text{eff}}) \times \boldsymbol{\xi}_i$	ms^{-1}
$\boldsymbol{\tau}_i^{\text{eff}}$	$\boldsymbol{\tau} + \sum_j \boldsymbol{\tau}_{ij}(r_{ij})$	MPa
B	$(2.7 + 0.008T) \times 10^{-5}$	Pa s
$\Delta H(\tau_i(\theta))$	$\Delta H_0 [1 - (\tau_i(\theta)/\tau_p)^p]^q$	eV
ΔH_0	0.69	eV
$\tau_i(\theta)$	$\mathbf{e}_x \cdot \boldsymbol{\tau}_i^{\text{eff}} \cdot \hat{\mathbf{n}}$	MPa
τ_p	258	MPa
p	1	–
q	1	–
f_{kn}	1.05×10^8	s^{-1}
θ_{MRSS}	$\pi/12$	rad

$f_{\text{kn}} = 1.05 \times 10^8 \text{ s}^{-1}$ compared with the reference value of $f_{\text{kn}} = 2.31 \times 10^9 \text{ s}^{-1}$. The difference between these values most likely originating from the method of determining the kink-pair nucleation enthalpy, which will be described as follows.

Making the assumptions of both a constant activation volume and that the kink-pair is fully formed at the saddle point, we have

$$\begin{aligned}
 V = \text{const} &= - \left(\frac{\partial \Delta H}{\partial \tau_i} \right)_T = - \frac{\partial}{\partial \tau_i} \left\{ \Delta H_0 \left[1 - \left(\frac{\tau_i}{\tau_p} \right)^p \right]^q \right\} \\
 &= \frac{\Delta H_0}{\tau_p}, \tag{4.1}
 \end{aligned}$$

as it must be the case that $p = q = 1$ for a constant V . From the second assumption, we must have $V = 30b^2h$, as the area swept out by the nucleating kink-pair is $30bh$.

The Peierls stress is then

$$\tau_p = \frac{\Delta H_0}{30b^2h} \simeq 258 \text{ MPa.} \quad (4.2)$$

The assumptions made are oversimplifications: the activation volume does depend on stress (cf. Figure 2.1(b)) and a kink-pair is always a bulge at the saddle point in a high stress regime (cf. Section 2.2.1). A more physical assumption for the size of the critical bulge would have been to assume that the kink-pair is half formed at the saddle-point (resulting in a Peierls stress twice as large); however, it was found that the former led to results that were more consistent with the reference data.

The simulations were set up for non-symmetrical triple slip conditions: the MRSS plane cuts the base ($\bar{1}10$) plane/ y -axis with $\theta_{\text{MRSS}} = 15^\circ$ (see Figure 3.4), such that slip occurs mainly on ‘a’ , planes, is less likely on ‘b’ planes and is least likely on ‘c’ planes. The results of the simulations were each obtained with a minimum of 10^5 kMC steps with each kMC step consisting of a minimum of 10 segment moves, assuming a single kink-pair on the dislocation line at any one time with $x_{\text{mig}} = 5b$. Running on a 3 GHz 20 MB cache i7 processor, 10^5 kMC steps took ≈ 135 hrs to complete. The results are shown in Table 4.2, with the obtained values being the average dislocation velocity magnitude over a simulation. As can be seen, the obtained velocities are in good agreement with the reference values, with the largest discrepancies occurring for $\tau = 200\text{MPa}$. A feature of the simulations for $\tau = 200\text{MPa}$ was that the kink-pairs almost always nucleated on the primary ($\bar{1}10$) plane; this being due to the low Peierls stress being approached and the exponential dependence of the nucleation rates. In contrast with the reference results, however, no cross-kink formation was observed at $T = 400$ K with the kink migration times being $10^3 - 10^7$ times smaller than the nucleation times at this temperature.

The predicted values in the third column are those based on the total nucleation rate of an unknicked dislocation (initial rate), calculated using Equation (3.9). For glide on a single plane and with one kink-pair on the dislocation line at any one time the obtained values would equal the predicted values after infinitely many kMC steps (see footnote Section 1.2). This would be the case as the kMC simulation time would be composed of timesteps based on the initial rate, with the kink migration times making a negligible contribution. The percentage differences between the predicted

Table 4.2: Showing the simulation velocity data. The predicted values are based on the total nucleation rate of an unknicked dislocation, the obtained values are the results from kMC runs, and the percentages are the differences between the obtained and predicted values. The reference data are the pure iron velocities from Katzarov *et al*^[11].

T/K	τ/MPa	$v/\text{nm s}^{-1}$		
		Predicted	Obtained	Reference
150	50	3.68×10^{-9}	3.61×10^{-9} (1.9%)	4.13×10^{-9}
	100	7.49×10^{-5}	7.39×10^{-5} (1.3%)	4.69×10^{-5}
	200	35.0×10^3	34.7×10^3 (0.86%)	6.10×10^3
300	50	11.75	10.79 (8.2%)	10.65
	100	1.44×10^3	1.37×10^3 (4.9%)	1.10×10^3
	200	2.92×10^7	2.89×10^7 (1.0%)	1.25×10^7
400	50	2.96×10^3	2.53×10^3 (15%)	2.46×10^3
	100	9.96×10^4	9.49×10^4 (4.7%)	7.68×10^4
	200	15.9×10^7	14.8×10^7 (6.9%)	8.38×10^7

Table 4.3: Showing simulation velocity data in nm s^{-1} for different values of θ_{MRSS} . The values in parentheses are the predicted velocities based on the initial rate.

	1 Plane	$\theta_{\text{MRSS}} = 0$	$\theta_{\text{MRSS}} = 15^\circ$	$\theta_{\text{MRSS}} = 30^\circ$
300 K 50MPa	10.67(10.88)	11.30(12.52)	10.79(11.75)	9.22(10.95)
400 K 200MPa	$2.37(2.65) \times 10^8$	$2.37(2.65) \times 10^8$	$1.48(1.59) \times 10^8$	$6.06(6.64) \times 10^7$

and obtained values in Table 4.2 are consistent with convergence to the predicted values. The percentage differences decrease with increasing stress in all but one case. This is due to dislocation cross-slipping less with increasing stress (though, the number of cross-slip events increases with temperature), and so the motion becoming more planar. When the dislocation cross-slips it can go back on itself (in the z -direction), which leads to a lower average velocity. The discrepancy in the trend in the percentage differences occurs for $T = 400\text{K}$ and $\tau = 200\text{MPa}$. This is because there are extra kink-pair nucleation events at this temperature and level of stress, in contrast with the other temperatures and levels of stress where the single kink-pair dynamic applies. The extra kink-pair nucleation events serving to reduce the average velocity compared with the single kink-pair case, which is assumed for the predicted values.

Table 4.3 shows obtained dislocation velocities for different values of θ_{MRSS} and also for when the dislocation is restricted to one plane only. The values in parentheses are the predicted velocities based on the initial rate. The 300 K 50 MPa velocity for motion on a single plane is the closest of the results to its predicted value, as the dislocation doesn't get slowed by cross-slipping events. It's predicted velocity is also the lowest of the 300 K results, as the initial nucleation rate doesn't have contributions from event rates for transitions to other planes. A general trend in the results is that the velocities, both predicted and obtained, decrease as θ_{MRSS} increases. This is due to both an increased frequency of cross-slip events and due to the applied stress becoming less effective. Only when $\theta_{\text{MRSS}} = 0$ is the applied stress focused completely on one plane; in other cases, the τ_{xy} component is focused on a plane of constant y , and this is not a slip plane. Therefore, some of the applied stress is "wasted." The low Peierls stress being approached accentuates this "wasted" stress effect in the 400 K values, where the $\theta_{\text{MRSS}} = 0$ values are ≈ 4 times greater than the $\theta_{\text{MRSS}} = 30^\circ$ values.

4.2 Comparison with Reference Data II

In this section the results of testing the model against the pure iron velocity data from Shinzato *et al*^[13] will be presented.

The Shinzato *et al* kMC model is two-dimensional only (i.e. glide occurs on a single plane) and kink migration is defined by a constant rate with a zero energy barrier for pure iron, so that at each kMC step either a nucleation event or a migration event is chosen according to their probabilities. Also, the activation energies in this model include a linear dependence on temperature. The parameters used and functional dependencies are shown in Table 4.4. The same lattice parameter, value of h , 300 K shear modulus and Poisson's ratio are used as previously for convenience, and the constant velocity method of kink migration is retained. The core cut-off parameter in this case was calibrated such that the excess energy of a dislocation with a kink-pair of $L = 25b$ was 0.64 eV, which gave $r_c = 0.323b$.

The results are shown in Table 4.5, with each result being obtained with 10^4 kMC steps. The column headings have the same meaning as for Table 4.2; however,

Table 4.4: List of parameters and functional dependencies used in testing the model against the Shinzato *et al* reference data. T_m is the melting point of iron.

Parameter	Value or Function	Units
a_0	2.87	Å
b	$a_0\sqrt{3}/2$	Å
h	2.31	Å
μ	71	GPa
ν	0.28	–
r_c	0.323	b
x_{mig}	5	b
L	20	b
L_D	1000	b
\mathbf{v}_{k_i}	$\pm b\tau_{i,xz}^{\text{eff}} \mathbf{e}_x / B$	m s^{-1}
$\tau_{i,xz}^{\text{eff}}$	$\tau_{xz} + \sum_j \tau_{xz}^{ij}(r_{ij})$	MPa
B	$(2.7 + 0.008T) \times 10^{-5}$	Pa s
$\Delta G(\tau_{i,xz}^{\text{eff}}, T)$	$(\Delta H_0 [1 - (\tau_{i,xz}^{\text{eff}}/\tau_p)^p]^q) (1 - T/T_m)$	eV
ΔG_0	0.64	eV
τ_p	1184	MPa
T_m	1811	K
p	0.687	–
q	1.372	–
f_{kn}	2.0×10^{10}	s^{-1}

the values in parentheses now give the simulation average number of kink-pairs on the dislocation line N_{kp} . The reference data were obtained from a logarithmic plot. The predicted values are consistent with the reference data, and so are the obtained values where $N_{\text{kp}} \approx 1$. Where $N_{\text{kp}} > 2$ the obtained values differ from the predicted and reference values by approximately an order of magnitude. As explained in Section 3.3, more kink-pairs on the dislocation line serve to reduce v compared with the single kink-pair dynamic. The predicted values (II) in Table 4.6 use Equations (3.9) and (3.10) to calculate v based on c_{kp} and the average rate J . As can be seen, there is good agreement between these predicted values and the obtained ones. The predicted values I are those from Table 4.5. Shinzato *et al* claim that they obtain a linear relation for dislocation glide in pure Fe from their simulations, and extract the activation enthalpies for each stress level from the slopes of their logarithmic plots. Indeed this is the case using the predicted (I) velocities, which are plotted in Figure

Table 4.5: Showing the simulation velocity data. The predicted values are based on the initial rate, the obtained values are the results from kMC runs, and the values in parentheses are the simulation average number of kink-pairs on the dislocation line. The reference data are the pure iron velocities from Shinzato *et al*^[13], which were obtained from a logarithmic plot.

T/K	τ/MPa	$v/\text{m s}^{-1}$		
		Predicted	Obtained	Reference
50	100	1.36×10^{-44}	1.26×10^{-44} (1.00)	$\approx 10^{-44}$
	500	7.74×10^{-18}	8.39×10^{-18} (1.00)	$\approx 10^{-19}$
	1000	4.42	4.46 (1.02)	$\approx 10^1$
100	100	3.75×10^{-20}	3.75×10^{-20} (1.00)	$10^{-20} < v < 10^{-19}$
	500	3.73×10^{-7}	4.01×10^{-7} (1.00)	$\approx 10^{-7}$
	1000	1.58×10^2	39.3 (2.72)	$\approx 10^2$
200	100	6.22×10^{-8}	5.98×10^{-8} (1.00)	$10^{-8} < v < 10^{-7}$
	500	8.19×10^{-2}	9.18×10^{-2} (1.00)	$10^{-2} < v < 10^{-1}$
	1000	9.42×10^2	85.1 (6.48)	$\approx 10^3$
300	100	7.37×10^{-4}	7.54×10^{-4} (1.00)	$\approx 10^{-3}$
	500	4.94	3.25 (1.13)	$10^0 < v < 10^1$
	1000	1.71×10^3	1.09×10^2 (9.52)	$10^3 < v < 10^4$
400	100	8.02×10^{-2}	8.79×10^{-2} (1.00)	$\approx 10^{-1}$
	500	38.4	10.8 (2.53)	$10^1 < v < 10^2$
	1000	2.30×10^3	1.17×10^2 (11.0)	$10^3 < v < 10^4$

Table 4.6: Showing for $\tau = 1000$ MPa the predicted velocities based on the initial rate (I), the predicted velocities based on Equations (3.9) and (3.10) (II), the obtained simulation velocities, the simulation average number of kink-pairs and the simulation average nucleation rate.

T/K	Predicted I $v/\text{m s}^{-1}$	Predicted II $v/\text{m s}^{-1}$	Obtained $v/\text{m s}^{-1}$	Avg. No. Kink-Pairs	Avg. Rate/ $\text{m}^{-1} \text{s}^{-1}$
100	1.58×10^2	38.7	39.3	2.72	2.51×10^{18}
200	9.42×10^2	95.2	85.1	6.48	1.24×10^{19}
300	1.71×10^3	1.06×10^2	1.09×10^2	9.52	1.94×10^{19}
400	2.30×10^3	1.16×10^2	1.17×10^2	11.0	2.40×10^{19}

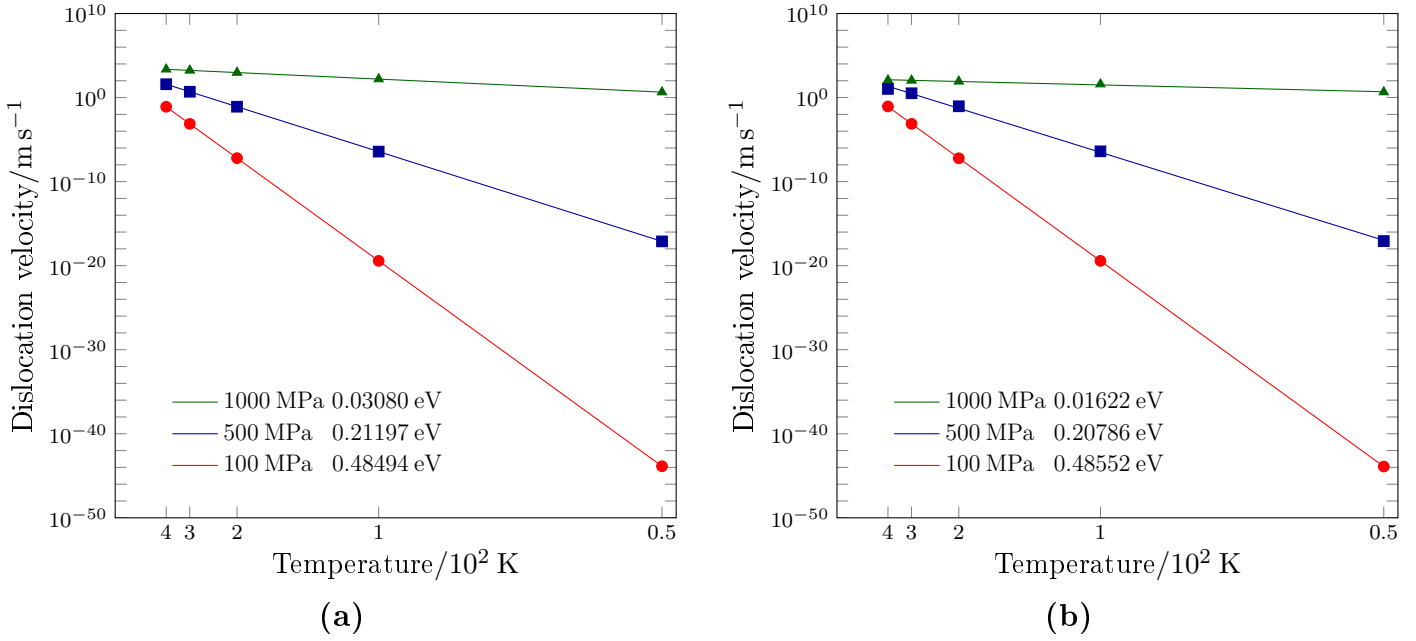


Figure 4.1: Showing (a) plots of the predicted dislocation velocities based on the initial rate against inverse temperature and (b) plots of the velocities obtained from simulations against inverse temperature. The legend in both cases shows the applied stress level and the slopes of the plots in eV, which are calculated using Equation (4.7).

4.1(a) against inverse temperature, with the activation enthalpies extracted from the slopes noted in the legend. These values can be verified using the expression for ΔG and the relevant parameters in Table 4.4 (with $T = 0$). The slope gives the activation enthalpy, as from the Gibbs–Helmholtz equation for a constant stress

$$\left(\frac{\partial(\Delta G/T)}{\partial T}\right)_\tau = -\frac{\Delta H}{T^2}, \quad (4.3)$$

and the relation between the velocity and activation energy^[2]

$$v = v_0 \exp\left(-\frac{\Delta G}{k_B T}\right) \Rightarrow \Delta G = -k_B T \ln\left(\frac{v}{v_0}\right), \quad (4.4)$$

we have

$$\frac{\partial(\Delta G/T)}{\partial T} = -k_B \frac{\partial}{\partial T} \left[\ln\left(\frac{v}{v_0}\right) \right] = -\frac{\Delta H}{T^2}, \quad (4.5)$$

assuming that the velocity prefactor v_0 is temperature independent and integrating

$$-k_B \ln v = \frac{\Delta H}{T} + C, \quad (4.6)$$

and then differentiating with respect to $1/T$, we obtain

$$-k_B \left(\frac{\partial(\ln v)}{\partial(1/T)} \right)_\tau = \Delta H. \quad (4.7)$$

However, at high levels of stress this relationship breaks down, as $N_{\text{kp}} > 2$. Figure 4.1(b) shows plots of actual simulation data, with the legend showing the slopes in terms of eV once more. The slope of the $\tau = 1000$ MPa plot differs by $\approx 50\%$ from that in Figure 4.1(a), and so no longer gives the activation enthalpy. As a check on the simulation data, the dislocation velocity can be predicted using only the input parameters and the assumption of a steady state, which Shinzato *et al* state that their simulations reach. From Table 4.4, we have

$$\Delta G = \left(\Delta H_0 \left[1 - \left(\frac{\tau_{i,xz}^{\text{eff}}}{\tau_p} \right)^p \right]^q \right) \left(1 - \frac{T}{T_m} \right), \quad (4.8)$$

and the nucleation rate J per b is

$$J = f_{\text{kn}} \exp\left(-\frac{\Delta G}{k_B T}\right), \quad (4.9)$$

neglecting any internal stresses (i.e. equating $\tau_{i,xz}^{\text{eff}}$ with the applied stress) and using the parameters in Table 4.4, we obtain for $T = 400$ K and $\tau_{xz} = 1000$ MPa

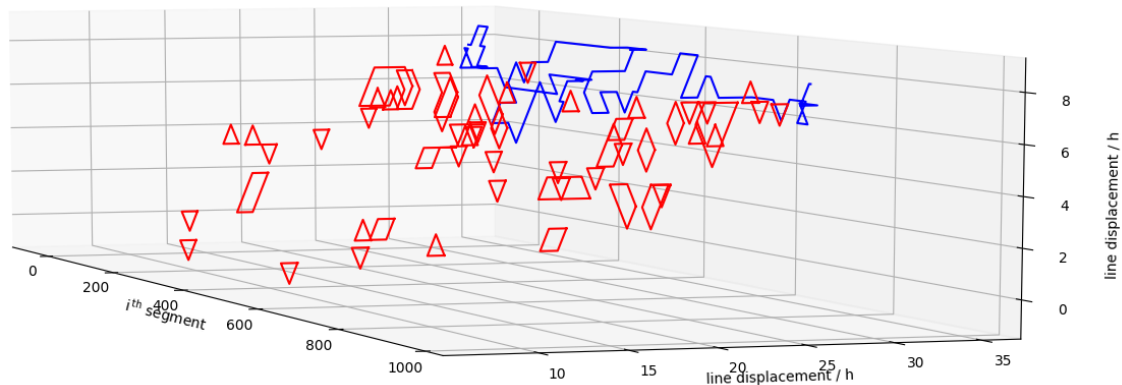
$$J = 9.9696 \times 10^9 b^{-1} \text{ s}^{-1} = 4.0111 \times 10^{19} \text{ m}^{-1} \text{ s}^{-1}. \quad (4.10)$$

Now, the kink speed is given by Equation (3.1):

$$v_k = \frac{\tau_{xz} b}{B} = 4212.7 \text{ m s}^{-1},$$

and using Equations (3.11) and (3.12), the predicted velocity is $v = 175.4 \text{ m s}^{-1}$, which is consistent with the predicted (II) and obtained velocities in Table 4.6. Although this result is greater than the latter, the average simulation rate will always be lower than the one just used in the calculation. Therefore, it must be the case that either the Shinzato *et al* kMC simulations are flawed or they simply just calculated the velocities using the initial rate without taking into account the presence of multiple kink-pairs to obtain their pure iron data.

Figure 4.2: Showing a three-dimensional simulation plot of a kinked dislocation line in blue and trailing debris loops in red



4.3 General

Further results from tests, which used the parameters in Table 4.1, are reported in this section. As no cross-kink or debris loop formation was observed for $p = q = 1$, tests were also carried out with $p = 0.2$ and $q = 2$, with this adjustment increasing the nucleation rates such that the kink migration times and the nucleation times became of the same order of magnitude. Table 4.7 shows the obtained simulation velocity for this case and with $T = 400$ K and $\tau = 50$ MPa. The obtained velocity is

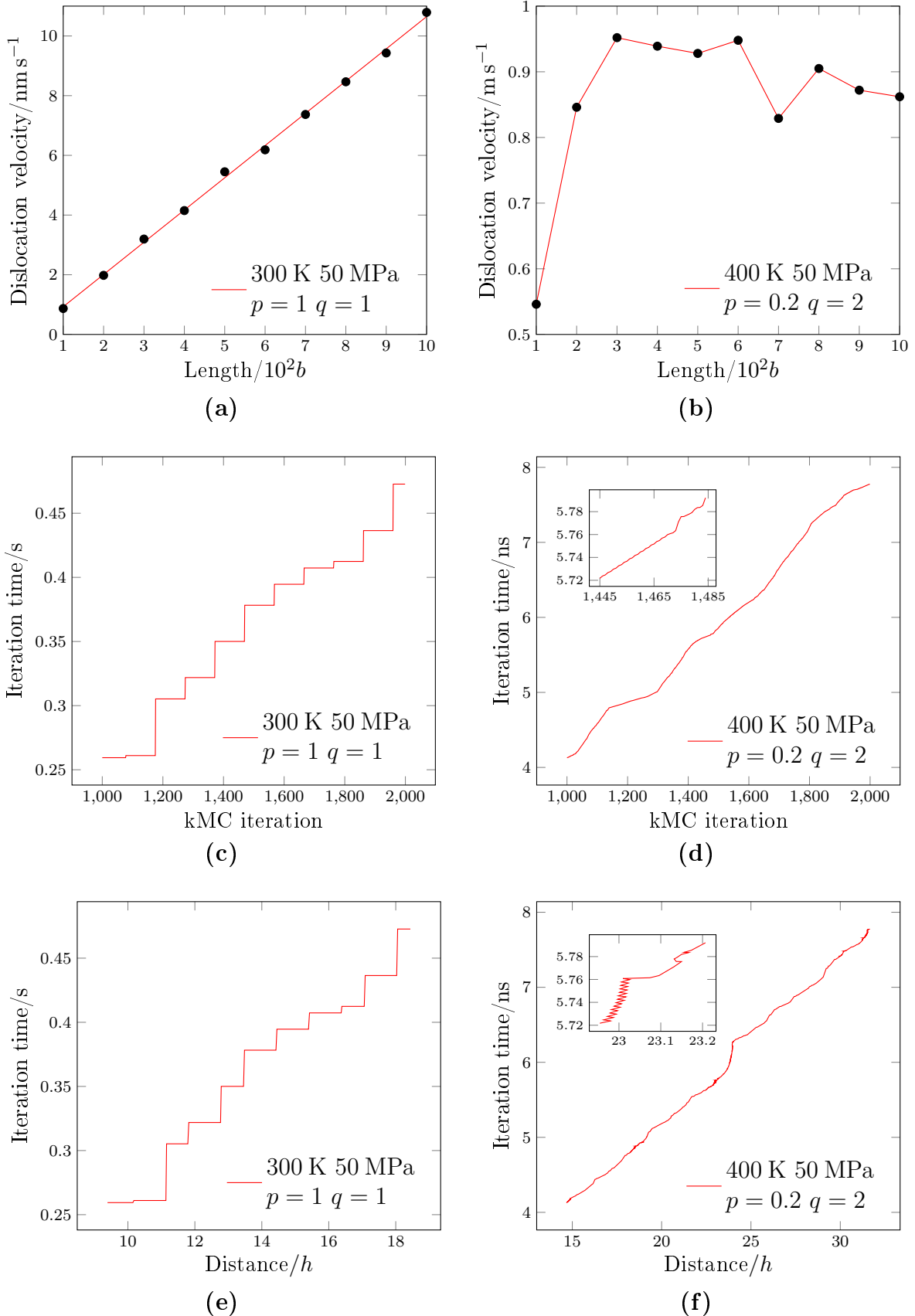
Table 4.7: Obtained velocity for $p = 0.2$, $q = 2$, $T = 400$ K and $\tau = 50$ MPa. The predicted velocity is that based on the initial rate.

	Obtained	Predicted (I)
Velocity/ m s^{-1}	0.862	7.983

less than the predicted (I) velocity based on the initial rate, due to increased kink-pair nucleation and also due to the formation of cross-kinks and kink pile-ups, which act as pinning points. Figure 4.2 shows a simulation plot of a kinked dislocation line in blue and trailing debris loops in red, which result from the dislocation “breaking free” from the pile-ups. A consequence of the increased number of kinks is that the simulations took ≈ 300 times longer to complete compared with those described in Section 4.1, with 10^4 kMC iterations taking ≈ 15 days to complete in some cases. This is because the interactions of each kink with every other kink and screw segment must be calculated.

Figure 4.3 shows plots for an applied stress of 50 MPa and for temperatures of

Figure 4.3: Showing plots for an applied stress of 50 MPa and for temperatures of 300 K with $p = q = 1$ in (a), (c) and (e); and for 400 K with $p = 0.2$ and $q = 2$ in (b), (d) and (f). Dislocation velocity versus length is shown in (a) and (b), kMC timestep versus iteration number is shown in (c) and (d), and the corresponding kMC timestep versus average dislocation position plots are shown in (e) and (f). The inset plots in (d) and (f) show enlarged areas, which both correspond to the same time frame.



300 K with $p = q = 1$ in (a), (c) and (e); and for 400 K with $p = 0.2$ and $q = 2$ in (b), (d) and (f). Dislocation velocity versus length is shown in (a) and (b). In (a) the single kink-pair dynamic rules the motion of the dislocation, and so the velocity is proportional to the number of nucleation sites, which increases with length. This relationship breaks down in (b) in a situation where there are multiple kink-pairs on the dislocation line at any one time. The velocity is seen to increase to a maximum at $l = 300b$ and then decrease on average above this length, due to increased kink-pair nucleation, cross-kink formation and the development of kink pile-ups. It must be noted that less kMC steps were used to obtain the data in (b). In (c) and (d) the kMC simulation time step versus iteration number is shown for a subset of iterations. The vertical portions of the plot in (c) show the kink-pair nucleation events, while the kink migration events are the horizontal portions. This illustrates the orders of magnitude time difference between these events in this regime ruled by the single kink-pair dynamic, where kink migration is practically instant compared with the nucleation time. For the situation in (d), where these events are of the same order of magnitude, they can only be (barely) distinguished in the magnified portion of the plot in the inset figure. The plot in (e) shows iteration time versus average dislocation position corresponding to the plot in (c). It is almost identical in form to that in (c) with most of the distance being covered by the fast kink migration events. The vertical portions are now slightly slanted compared with those in (c) due to 3% of the dislocation line moving forward in the nucleation events. Finally, the plot in (f) shows iteration time versus average position corresponding to the situation in (d). The magnified portion of the curve in the inset figure shows that the roughness in the plot corresponds to the dislocation frequently cross-slipping with its average position increasing and decreasing.

Chapter 5

Summary and Outlook

In summary, a kMC model for simulating screw dislocations in iron has been developed in this research project and introduced in this report. It has been shown that the model can produce results that are both consistent with those in the literature and those predicted by theory. The code for this model is available at github.com. The relevant theory for the kink-pair mechanism was developed in Chapter 2 and, using input parameters from the literature, it was shown that the analytic LT model coupled with a sinusoidal potential best described the kink formation energy. Also the stress intervals where the EI and LT model are valid and methods of approximating the frequency prefactor were discussed. In Chapter 3 previous kMC studies and the implementation of this kMC model were described. Also, theoretical equations for predicting dislocation velocity were introduced so that the results of simulations could be analysed. It was shown in Section 4.1 of the results that a simple model for the kink-pair activation enthalpy could numerically reproduce the pure iron velocity data from Katzarov *et al*^[11]. However, no cross-kink formation was observed for $T = 400$ K due to 3-7 orders of magnitude difference between the kink migration times and the kink-pair nucleation times, depending on the level of applied stress. In Section 4.2 it was shown that the model reproduced the pure iron results from Shinzato *et al*^[13]; however, with one exception. This exception at high stress levels highlighted an error in their data, which was confirmed by analysis with the theoretical velocity equations. Finally, in Section 4.3 some other results of interest were described, including how dislocation velocity varies with length in two different kink-pair dynamical regimes. In the single kink-pair dynamic velocity is

proportional to length, with this relationship breaking down in the multiple kink-pair dynamic. The results in all sections were found to be consistent with theory.

This model provides a foundation for future research in this area in which the interactions between carbon solutes and dislocations will be investigated. The model needing only parameterisation from atomistic calculations so that the variation of dislocation velocity with various levels of temperature, applied stress and carbon concentration can be determined. The atomistic calculations can be performed via the nudged elastic band (NEB)[†] method where the activation enthalpy for kink-pair nucleation will be determined for various concentrations and positions of carbon. The results can be implemented in the model using the method of Deo *et al*^[20], which was described in Section 3.1. Non-Schmid effects can also be included in the model, using the results of similar atomistic calculations with varying configurations of the applied stress tensor. This model can also be easily adapted for other bcc metals.

Lastly, although the Python programming language, in which this model is coded, is convenient – being easy to read and write – it is also very inefficient when it comes to programming loops. The kink and dislocation line segment interactions are all calculated with the use of loops, and, as noted in Section 4.3, the simulations can become very slow. Ultimately, to improve performance, the slowest parts of the code will have to be rewritten in another programming language such as C++ and then an application such as SWIG can be used to integrate the original and rewritten parts of the code.

[†]The NEB method finds the minimum energy path (MEP) connecting initial and final atomic configurations by optimizing a number of intermediate images along the reaction path.

Bibliography

- [1] World Steel Association, *World Steel in Figures*, E. Basson, Ed. World Steel Association, 2020. [Online]. Available: <https://www.worldsteel.org/steel-by-topic/statistics/World-Steel-in-Figures.html>
- [2] P. M. Anderson, J. P. Hirth, and J. Lothe, *Theory of Dislocations*, 3rd ed. Cambridge University Press, 2017. [Online]. Available: <https://www.cambridge.org/gb/academic/subjects/engineering/materials-science/theory-dislocations-3rd-edition?format=HB&isbn=9780521864367>
- [3] L. Landau and E. Lifshitz, *Theory of Elasticity*, third edition ed., E. Lifshitz, A. Kosevich, and L. Pitaevskii, Eds. Oxford: Butterworth-Heinemann, 1986. [Online]. Available: <http://www.sciencedirect.com/science/article/pii/B9780080570693500085>
- [4] M. Tang, L. Kubin, and G. Canova, “Dislocation mobility and the mechanical response of b.c.c. single crystals: A mesoscopic approach,” *Acta Materialia*, vol. 46, no. 9, pp. 3221 – 3235, 1998. [Online]. Available: <http://www.sciencedirect.com/science/article/pii/S1359645498000068>
- [5] V. Bulatov, F. F. Abraham, L. Kubin, B. Devincre, and S. Yip, “Connecting atomistic and mesoscale simulations of crystal plasticity,” *Nature*, vol. 391, no. 6668, pp. 669–672, Feb 1998. [Online]. Available: <https://doi.org/10.1038/35577>
- [6] V. Bulatov and W. Cai, *Computer Simulations of Dislocations*, ser. Oxford Series on Materials Modelling. New York, NY, USA: Oxford University Press, Inc., 2006. [Online]. Available: <https://global.oup.com/academic/product/computer-simulations-of-dislocations-9780199674060?cc=gb&lang=en&#>
- [7] A. Bortz, M. Kalos, and J. Lebowitz, “A new algorithm for Monte Carlo simulation of Ising spin systems,” *Journal of Computational Physics*, vol. 17, no. 1, pp. 10 – 18, 1975. [Online]. Available: <http://www.sciencedirect.com/science/article/pii/0021999175900601>
- [8] D. Gillespie, *Markov Processes: An Introduction for Physical Scientists*, first edition ed. San Diego: Academic Press, 1992. [Online]. Available: <http://www.sciencedirect.com/science/article/pii/B9780080918372500041>
- [9] A. F. Voter, “Introduction to the kinetic monte carlo method,” in *Radiation Effects in Solids*, K. E. Sickafus, E. A. Kotomin, and B. P. Uberuaga, Eds. Dordrecht: Springer Netherlands, 2007, pp. 1–23. [Online]. Available: https://link.springer.com/chapter/10.1007%2F978-1-4020-5295-8_1

- [10] E. Orowan, “Zur Kristallplastizität. III,” *Zeitschrift für Physik*, vol. 89, no. 9, pp. 634–659, Sep 1934. [Online]. Available: <https://doi.org/10.1007/BF01341480>
- [11] I. H. Katzarov, D. L. Pashov, and A. T. Paxton, “Hydrogen embrittlement I. Analysis of hydrogen-enhanced localized plasticity: Effect of hydrogen on the velocity of screw dislocations in α -Fe,” *Phys. Rev. Materials*, vol. 1, p. 033602, Aug 2017. [Online]. Available: <https://link.aps.org/doi/10.1103/PhysRevMaterials.1.033602>
- [12] Y. Zhao and J. Marian, “Direct prediction of the solute softening-to-hardening transition in W–Re alloys using stochastic simulations of screw dislocation motion,” *Modelling and Simulation in Materials Science and Engineering*, vol. 26, no. 4, p. 045002, mar 2018. [Online]. Available: <https://doi.org/10.1088%2F1361-651x%2Faaecf>
- [13] S. Shinzato, M. Wakeda, and S. Ogata, “An atomistically informed kinetic Monte Carlo model for predicting solid solution strengthening of body-centered cubic alloys,” *International Journal of Plasticity*, vol. 122, pp. 319 – 337, 2019. [Online]. Available: <http://www.sciencedirect.com/science/article/pii/S0749641918307356>
- [14] N. Metropolis, A. W. Rosenbluth, M. N. Rosenbluth, A. H. Teller, and E. Teller, “Equation of State Calculations by Fast Computing Machines,” *The Journal of Chemical Physics*, vol. 21, no. 6, pp. 1087–1092, 1953. [Online]. Available: <https://doi.org/10.1063/1.1699114>
- [15] A. Argon, *Strengthening Mechanisms in Crystal Plasticity*, ser. Oxford Series on Materials Modelling. Oxford University Press, 2007. [Online]. Available: <https://oxford.universitypressscholarship.com/view/10.1093/acprof:oso/9780198516002.001.0001/acprof-9780198516002>
- [16] G. Schoeck, “The Activation Energy of Dislocation Movement,” *physica status solidi (b)*, vol. 8, no. 2, pp. 499–507, 1965. [Online]. Available: <https://onlinelibrary.wiley.com/doi/abs/10.1002/pssb.19650080209>
- [17] U. Kocks, A. Argon, and M. Ashby, *Thermodynamics and Kinetics of Slip*, ser. Progress in materials science. Pergamon Press, 1975. [Online]. Available: <https://www.sciencedirect.com/journal/progress-in-materials-science/vol/19/suppl/C>
- [18] G. H. Vineyard, “Frequency factors and isotope effects in solid state rate processes,” *Journal of Physics and Chemistry of Solids*, vol. 3, no. 1, pp. 121 – 127, 1957. [Online]. Available: <http://www.sciencedirect.com/science/article/pii/0022369757900598>
- [19] K. Lin and D. C. Chrzan, “Kinetic Monte Carlo simulation of dislocation dynamics,” *Phys. Rev. B*, vol. 60, pp. 3799–3805, Aug 1999. [Online]. Available: <https://link.aps.org/doi/10.1103/PhysRevB.60.3799>

- [20] C. Deo, D. Srolovitz, W. Cai, and V. Bulatov, “Stochastic simulation of dislocation glide in tantalum and Ta-based alloys,” *Journal of the Mechanics and Physics of Solids*, vol. 53, no. 6, pp. 1223 – 1247, 2005. [Online]. Available: <http://www.sciencedirect.com/science/article/pii/S0022509605000189>
- [21] A. Stukowski, D. Cereceda, T. D. Swinburne, and J. Marian, “Thermally-activated non-Schmid glide of screw dislocations in W using atomistically-informed kinetic Monte Carlo simulations,” *International Journal of Plasticity*, vol. 65, pp. 108 – 130, 2015. [Online]. Available: <http://www.sciencedirect.com/science/article/pii/S074964191400182X>
- [22] D. Hull and D. Bacon, *Introduction to Dislocations (Fifth Edition)*, fifth edition ed. Oxford: Butterworth-Heinemann, 2011. [Online]. Available: <https://www.sciencedirect.com/book/9780080966724/introduction-to-dislocations>
- [23] E. Schmid and W. Boas, *Kristallplastizität: Mit Besonderer Berücksichtigung der Metalle*, ser. Struktur und Eigenschaften der Materie in Einzeldarstellungen. Berlin, Heidelberg: Springer-Verlag Berlin Heidelberg, 1935, vol. 17. [Online]. Available: https://doi.org/10.1007/978-3-662-34532-0_2
- [24] A. Seeger, “Why anomalous slip in body-centred cubic metals?” *Materials Science and Engineering: A*, vol. 319-321, pp. 254 – 260, 2001. [Online]. Available: <http://www.sciencedirect.com/science/article/pii/S0921509301009583>
- [25] D. Rodney and L. Proville, “Stress-dependent Peierls potential: Influence on kink-pair activation,” *Phys. Rev. B*, vol. 79, p. 094108, Mar 2009. [Online]. Available: <https://link.aps.org/doi/10.1103/PhysRevB.79.094108>
- [26] R. Gröger and V. Vitek, “Stress dependence of the Peierls barrier of $1/2\langle 111 \rangle$ screw dislocations in bcc metals,” *Acta Materialia*, vol. 61, no. 17, pp. 6362 – 6371, 2013. [Online]. Available: <http://www.sciencedirect.com/science/article/pii/S1359645413004886>
- [27] M. Peach and J. S. Koehler, “The Forces Exerted on Dislocations and the Stress Fields Produced by Them,” *Phys. Rev.*, vol. 80, pp. 436–439, Nov 1950. [Online]. Available: <https://link.aps.org/doi/10.1103/PhysRev.80.436>
- [28] J. W. Christian, “Some surprising features of the plastic deformation of body-centered cubic metals and alloys,” *Metallurgical Transactions A*, vol. 14, no. 7, pp. 1237–1256, Jul 1983. [Online]. Available: <https://doi.org/10.1007/BF02664806>
- [29] C. R. Weinberger, B. L. Boyce, and C. C. Battaile, “Slip planes in bcc transition metals,” *International Materials Reviews*, vol. 58, no. 5, pp. 296–314, 2013. [Online]. Available: <https://doi.org/10.1179/1743280412Y.0000000015>
- [30] V. Vitek, “Core structure of screw dislocations in body-centred cubic metals: relation to symmetry and interatomic bonding,” *Philosophical Magazine*, vol. 84, no. 3-5, pp. 415–428, 2004. [Online]. Available: <https://doi.org/10.1080/14786430310001611644>

- [31] E. Clouet, L. Ventelon, and F. Willaime, “Dislocation core energies and core fields from first principles,” *Phys. Rev. Lett.*, vol. 102, p. 055502, Feb 2009. [Online]. Available: <https://link.aps.org/doi/10.1103/PhysRevLett.102.055502>
- [32] M. Itakura, H. Kaburaki, and M. Yamaguchi, “First-principles study on the mobility of screw dislocations in bcc iron,” *Acta Materialia*, vol. 60, no. 9, pp. 3698 – 3710, 2012. [Online]. Available: <http://www.sciencedirect.com/science/article/pii/S1359645412002236>
- [33] C. R. Weinberger, G. J. Tucker, and S. M. Foiles, “Peierls potential of screw dislocations in bcc transition metals: Predictions from density functional theory,” *Phys. Rev. B*, vol. 87, p. 054114, Feb 2013. [Online]. Available: <https://link.aps.org/doi/10.1103/PhysRevB.87.054114>
- [34] D. Cereceda, M. Diehl, F. Roters, P. Shanthraj, D. Raabe, J. M. Perlado, and J. Marian, “Linking atomistic, kinetic monte carlo and crystal plasticity simulations of single-crystal tungsten strength,” *GAMM-Mitteilungen*, vol. 38, no. 2, pp. 213–227, 2015. [Online]. Available: <https://onlinelibrary.wiley.com/doi/abs/10.1002/gamm.201510012>
- [35] D. Rodney, L. Ventelon, E. Clouet, L. Pizzagalli, and F. Willaime, “Ab initio modeling of dislocation core properties in metals and semiconductors,” *Acta Materialia*, vol. 124, pp. 633 – 659, 2017. [Online]. Available: <http://www.sciencedirect.com/science/article/pii/S1359645416307492>
- [36] W. Cai, V. V. Bulatov, J. Chang, J. Li, and S. Yip, “Chapter 64 - dislocation core effects on mobility,” in *Dislocations in Solids*, ser. Dislocations in Solids, F. Nabarro and J. Hirth, Eds. Elsevier, 2004, vol. 12, pp. 1 – 80. [Online]. Available: <http://www.sciencedirect.com/science/article/pii/S1572485905800038>
- [37] D. Caillard, “Kinetics of dislocations in pure Fe. Part I. In situ straining experiments at room temperature,” *Acta Materialia*, vol. 58, no. 9, pp. 3493 – 3503, 2010. [Online]. Available: <http://www.sciencedirect.com/science/article/pii/S1359645410001096>
- [38] D. Caillard, “Kinetics of dislocations in pure Fe. Part II. In situ straining experiments at low temperature,” *Acta Materialia*, vol. 58, no. 9, pp. 3504 – 3515, 2010. [Online]. Available: <http://www.sciencedirect.com/science/article/pii/S1359645410001102>
- [39] C. Marichal, H. Van Swygenhoven, S. Van Petegem, and C. Borca, “ $\{110\}$ Slip with $\{112\}$ slip traces in bcc Tungsten,” *Scientific Reports*, vol. 3, no. 1, p. 2547, Aug 2013. [Online]. Available: <https://doi.org/10.1038/srep02547>
- [40] R. Gröger, A. Bailey, and V. Vitek, “Multiscale modeling of plastic deformation of molybdenum and tungsten: I. atomistic studies of the core structure and glide of $1/2\langle 111 \rangle$ screw dislocations at 0k,” *Acta Materialia*, vol. 56, no. 19, pp. 5401 – 5411, 2008. [Online]. Available: <http://www.sciencedirect.com/science/article/pii/S1359645408005132>

- [41] R. Gröger, V. Racherla, J. Bassani, and V. Vitek, “Multiscale modeling of plastic deformation of molybdenum and tungsten: ii. yield criterion for single crystals based on atomistic studies of glide of $1/2\langle 111 \rangle$ screw dislocations,” *Acta Materialia*, vol. 56, no. 19, pp. 5412 – 5425, 2008. [Online]. Available: <http://www.sciencedirect.com/science/article/pii/S1359645408005144>
- [42] R. Gröger and V. Vitek, “Multiscale modeling of plastic deformation of molybdenum and tungsten. iii. effects of temperature and plastic strain rate,” *Acta Materialia*, vol. 56, no. 19, pp. 5426 – 5439, 2008. [Online]. Available: <http://www.sciencedirect.com/science/article/pii/S1359645408005156>
- [43] K. Srivastava, R. Gröger, D. Weygand, and P. Gumbsch, “Dislocation motion in tungsten: Atomistic input to discrete dislocation simulations,” *International Journal of Plasticity*, vol. 47, pp. 126 – 142, 2013. [Online]. Available: <http://www.sciencedirect.com/science/article/pii/S0749641913000247>
- [44] M. Duesbery and V. Vitek, “Plastic anisotropy in b.c.c. transition metals,” *Acta Materialia*, vol. 46, no. 5, pp. 1481 – 1492, 1998. [Online]. Available: <http://www.sciencedirect.com/science/article/pii/S1359645497003674>
- [45] H. Lim, L. Hale, J. Zimmerman, C. Battaile, and C. Weinberger, “A multi-scale model of dislocation plasticity in α -Fe: Incorporating temperature, strain rate and non-Schmid effects,” *International Journal of Plasticity*, vol. 73, pp. 100 – 118, 2015, special Issue on Constitutive Modeling from Micro-Scale to Continuum in Honor of Prof. Frédéric Barlat. [Online]. Available: <http://www.sciencedirect.com/science/article/pii/S0749641914002356>
- [46] D. Caillard and J. Martin, *Thermally Activated Mechanisms in Crystal Plasticity*, ser. Pergamon Materials Series. Pergamon, 2003, vol. 8. [Online]. Available: <http://www.sciencedirect.com/science/article/pii/S1470180403800366>
- [47] W. Spitzig and A. Keh, “Orientation dependence of the strain-rate sensitivity and thermally activated flow in iron single crystals,” *Acta Metallurgica*, vol. 18, no. 9, pp. 1021 – 1033, 1970. [Online]. Available: <http://www.sciencedirect.com/science/article/pii/0001616070900581>
- [48] A. Seeger, “The kink picture of dislocation mobility and dislocation-point-defect interaction,” *Journal de Physique Colloque*, no. 5,pt1, pp. 201–228, 1981. [Online]. Available: http://inis.iaea.org/search/search.aspx?orig_q=RN:13690251
- [49] J. E. Dorn and S. Rajnak, “Nucleation of Kink Pairs and the Peierls’ Mechanism of Plastic Deformation,” 1963. [Online]. Available: https://scholar.google.com/scholar_lookup?title=Nucleation%20of%20kink%20Pairs%2BPeierls%20mechanism%20of%20plastic%20deformation&author=J.E.%20Dorn&publication_year=1964
- [50] L. Proville, L. Ventelon, and D. Rodney, “Prediction of the kink-pair formation enthalpy on screw dislocations in α -iron by a line tension model parametrized on empirical potentials and first-principles calculations,”

- Phys. Rev. B*, vol. 87, p. 144106, Apr 2013. [Online]. Available: <https://link.aps.org/doi/10.1103/PhysRevB.87.144106>
- [51] L. Dezerald, L. Proville, L. Ventelon, F. Willaime, and D. Rodney, “First-principles prediction of kink-pair activation enthalpy on screw dislocations in bcc transition metals: V, nb, ta, mo, w, and fe,” *Phys. Rev. B*, vol. 91, p. 094105, Mar 2015. [Online]. Available: <https://link.aps.org/doi/10.1103/PhysRevB.91.094105>
- [52] W. Spitzig, “Analysis of thermally-activated flow in iron single crystals,” *Acta Metallurgica*, vol. 18, no. 12, pp. 1275 – 1284, 1970. [Online]. Available: <http://www.sciencedirect.com/science/article/pii/0001616070901586>
- [53] D. Brunner and J. Diehl, “Strain-rate and temperature dependence of the tensile flow stress of high-purity α -iron above 250 k (regime i) studied by means of stress-relaxation tests,” *physica status solidi (a)*, vol. 124, no. 1, pp. 155–170, 1991. [Online]. Available: <https://onlinelibrary.wiley.com/doi/abs/10.1002/pssa.2211240114>
- [54] D. Brunner and J. Diehl, “Temperature and strain-rate dependence of the tensile flow stress of high-purity α -iron below 250 k. i. stress/temperature regime iii,” *physica status solidi (a)*, vol. 124, no. 2, pp. 455–464, 1991. [Online]. Available: <https://onlinelibrary.wiley.com/doi/abs/10.1002/pssa.2211240210>
- [55] E. Kubamoto, Y. Aono, K. Kitajima, K. Maeda, and S. Takeuchi, “Thermally activated slip deformation between 0.7 and 77 k in high-purity iron single crystals,” *Philosophical Magazine A*, vol. 39, no. 6, pp. 717–724, 1979. [Online]. Available: <https://doi.org/10.1080/01418617908239302>
- [56] L. Proville, D. Rodney, and M.-C. Marinica, “Quantum effect on thermally activated glide of dislocations,” *Nature Materials*, vol. 11, no. 10, pp. 845–849, Oct 2012. [Online]. Available: <https://doi.org/10.1038/nmat3401>
- [57] B. Barvinschi, L. Proville, and D. Rodney, “Quantum peierls stress of straight and kinked dislocations and effect of non-glide stresses,” *Modelling and Simulation in Materials Science and Engineering*, vol. 22, no. 2, p. 025006, jan 2014. [Online]. Available: <https://doi.org/10.1088/0965-0393/22/2/025006>
- [58] D. Brunner and J. Diehl, “Temperature and strain-rate dependence of the tensile flow stress of high-purity α -iron below 250 k ii. stress/temperature regime ii and its transitions to regimes i and iii,” *physica status solidi (a)*, vol. 125, no. 1, pp. 203–216, 1991. [Online]. Available: <https://onlinelibrary.wiley.com/doi/abs/10.1002/pssa.2211250117>
- [59] G. Schoeck, *Thermal Activation in Plastic Deformation*. Dordrecht: Springer Netherlands, 2000, pp. 33–56. [Online]. Available: https://doi.org/10.1007/978-94-011-4048-5_4
- [60] W. Cai, V. V. Bulatov, and S. Yip, “Kinetic monte carlo method for dislocation glide in silicon,” *Journal of Computer-Aided Materials*

- Design*, vol. 6, no. 2, pp. 175–183, May 1999. [Online]. Available: <https://doi.org/10.1023/A:1008730124719>
- [61] W. Cai, V. V. Bulatov, S. Yip, and A. S. Argon, “Kinetic Monte Carlo modeling of dislocation motion in BCC metals,” *Materials Science and Engineering: A*, vol. 309-310, pp. 270 – 273, 2001, dislocations 2000: An International Conference on the Fundamentals of Plastic Deformation. [Online]. Available: <http://www.sciencedirect.com/science/article/pii/S0921509300016890>
- [62] W. Cai, V. V. Bulatov, J. F. Justo, A. S. Argon, and S. Yip, “Kinetic monte carlo approach to modeling dislocation mobility,” *Computational Materials Science*, vol. 23, no. 1, pp. 124 – 130, 2002. [Online]. Available: <http://www.sciencedirect.com/science/article/pii/S0927025601002233>
- [63] I. Katzarov and A. Paxton, “Is the pinning of ordinary dislocations in γ -TiAl intrinsic or extrinsic in nature? A combined atomistic and kinetic Monte Carlo approach,” *Acta Materialia*, vol. 59, no. 3, pp. 1281 – 1290, 2011. [Online]. Available: <http://www.sciencedirect.com/science/article/pii/S1359645410007342>
- [64] G. Taylor, “Thermally-activated deformation of bcc metals and alloys,” *Progress in Materials Science*, vol. 36, pp. 29 – 61, 1992. [Online]. Available: <http://www.sciencedirect.com/science/article/pii/007964259290004Q>
- [65] F. C. Frank, “On the equations of motion of crystal dislocations,” *Proceedings of the Physical Society. Section A*, vol. 62, no. 2, pp. 131–134, feb 1949. [Online]. Available: <https://doi.org/10.1088%2F0370-1298%2F62%2F2%2F307>
- [66] J. J. Adams, D. S. Agosta, R. G. Leisure, and H. Ledbetter, “Elastic constants of monocrystal iron from 3to500k,” *Journal of Applied Physics*, vol. 100, no. 11, p. 113530, 2006. [Online]. Available: <https://aip.scitation.org/doi/abs/10.1063/1.2365714>
- [67] T. Y. Thomas, “On the stress-strain relations for cubic crystals,” *Proceedings of the National Academy of Sciences of the United States of America*, vol. 55, no. 2, pp. 235–239, 1966. [Online]. Available: <http://www.jstor.org/stable/57508>
- [68] K. M. Knowles and P. R. Howie, “The directional dependence of elastic stiffness and compliance shear coefficients and shear moduli in cubic materials,” *Journal of Elasticity*, vol. 120, no. 1, pp. 87–108, Jun 2015. [Online]. Available: <https://doi.org/10.1007/s10659-014-9506-1>
- [69] W. Cai, A. Arsenlis, C. R. Weinberger, and V. V. Bulatov, “A non-singular continuum theory of dislocations,” *Journal of the Mechanics and Physics of Solids*, vol. 54, no. 3, pp. 561 – 587, 2006. [Online]. Available: <http://www.sciencedirect.com/science/article/pii/S002250960500195X>
- [70] A. Y. Kuksin and A. V. Yanilkin, “Atomistic simulation of the motion of dislocations in metals under phonon drag conditions,” *Physics of the Solid State*, vol. 55, no. 5, pp. 1010–1019, May 2013. [Online]. Available: <https://doi.org/10.1134/S1063783413050193>

- [71] G. Po, Y. Cui, D. Rivera, D. Cereceda, T. D. Swinburne, J. Marian, and N. Ghoniem, “A phenomenological dislocation mobility law for bcc metals,” *Acta Materialia*, vol. 119, pp. 123 – 135, 2016. [Online]. Available: <http://www.sciencedirect.com/science/article/pii/S1359645416305948>

List of Figures

1.1	Illustrating the nucleation of a kink-pair. F represents the lattice potential, F_0 the dislocation free energy along the potential valley, L is the kink-pair width and λ is the distance between potential valleys ^[15] .	4
1.2	(a) A perfect simple cubic crystal. (b) Creation of an edge dislocation \perp by shearing the top half of the perfect crystal along the half plane A (solid line). A screw dislocation (c) and a mixed dislocation (d) ^[6] .	7
1.3	Illustration of the geometry of slip ^[22] .	10
2.1	“Two limiting forms of idealisation of a double kink on a screw dislocation: (a) at low stresses, where the double kink is made up of two well-separated, fully formed right-side and left-side kinks; (b) at high stresses, where the activation configuration is more in the form of a bulge that just places a portion of the line over the peak of the energy ridge ^[15] .”	15
2.2	Showing some simple model Peierls potentials. (Note that E here is U in the main text.) ^[46] .	18
2.3	“Equilibrium shape of an isolated kink (smooth potential) ^[46] .”	20
3.1	Illustrating the kMC events that describe screw dislocation glide in bcc metals ^[13] .	30
3.2	Schematic representation of a dislocation in a bcc metal in the kMC model. The dislocation line is mostly aligned along a $\langle 111 \rangle$ direction. Kink-pairs can nucleate on any of three types of $\{110\}$ plane a , b and c . A kink-pair nucleation event is shown at position I and a kink migration event is shown at position II, both in dashed lines ^[61] .	31
3.3	Schematic representation of the formation of (a) two kinks forming a cross-kink, (b) more kinks joining the cross-kink in a <i>pile-up</i> , and (c) debris loop L formation with the primary dislocation breaking away from the self-pinning point A. ^[61] .	31
3.4	“Schematic view of the glide planes of the $[111]$ zone. A generic MRSS plane is labeled in red, while, by way of example, the $(\bar{1}01)$ is the glide plane. ^[21] ”	35
4.1	Showing (a) plots of the predicted dislocation velocities based on the initial rate against inverse temperature and (b) plots of the velocities obtained from simulations against inverse temperature. The legend in both cases shows the applied stress level and the slopes of the plots in eV, which are calculated using Equation (4.7).	46

4.2	Showing a three-dimensional simulation plot of a kinked dislocation line in blue and trailing debris loops in red	48
4.3	Showing plots for an applied stress of 50 MPa and for temperatures of 300 K with $p = q = 1$ in (a), (c) and (e); and for 400 K with $p = 0.2$ and $q = 2$ in (b), (d) and (f). Dislocation velocity versus length is shown in (a) and (b), kMC timestep versus iteration number is shown in (c) and (d), and the corresponding kMC timestep versus average dislocation position plots are shown in (e) and (f). The inset plots in (d) and (f) show enlarged areas, which both correspond to the same time frame.	49

List of Tables

2.1	Showing the functional form of three of the potentials shown in Figure 2.2, along with their associated kink energies, calculated using Equation (2.30), and their Peierls stresses, found from their maximum gradient ^[46] .	22
2.2	Showing values for the kink-pair energy $2U_k$ and the Peierls stress τ_p in α -Fe, calculated using the three potentials and the formulae in Table 2.1. The parameters used were $b = 2.49 \text{ \AA}^{[11]}$, $h = 2.31 \text{ \AA}^{[11]}$, $\Delta U = 0.035 \text{ eV b}^{-1}$ ^[32] and $U_0 = 3.57 \text{ eV \AA}^{-1}$ ^[32,50,51] .	22
2.3	Showing the formulae and calculated values, using α -Fe parameters, of the estimates for f_{kn} discussed in this section. The parameters used were $\theta_D = 470 \text{ K}$ (note that h here is Planck's constant), $b = 2.49 \text{ \AA}$, $l = 30b$, the room temperature shear modulus ^[66] $\mu = 71 \text{ GPa}$, $\rho = 7874 \text{ kg m}^{-3}$, $y_s = 2.31 \text{ \AA}$ (i.e. the distance between Peierls valleys), $T = 300 \text{ K}$ and $U_0 \simeq T_L = 3.57 \text{ eV \AA}^{-1}$.	28
4.1	List of parameters and functional dependencies used in the kMC model.	40
4.2	Showing the simulation velocity data. The predicted values are based on the total nucleation rate of an unknicked dislocation, the obtained values are the results from kMC runs, and the percentages are the differences between the obtained and predicted values. The reference data are the pure iron velocities from Katzarov <i>et al</i> ^[11] .	42
4.3	Showing simulation velocity data in nm s^{-1} for different values of θ_{MRSS} . The values in parentheses are the predicted velocities based on the initial rate.	42
4.4	List of parameters and functional dependencies used in testing the model against the Shinzato <i>et al</i> reference data. T_m is the melting point of iron.	44
4.5	Showing the simulation velocity data. The predicted values are based on the initial rate, the obtained values are the results from kMC runs, and the values in parentheses are the simulation average number of kink-pairs on the dislocation line. The reference data are the pure iron velocities from Shinzato <i>et al</i> ^[13] , which were obtained from a logarithmic plot.	45
4.6	Showing for $\tau = 1000 \text{ MPa}$ the predicted velocities based on the initial rate (I), the predicted velocities based on Equations (3.9) and (3.10) (II), the obtained simulation velocities, the simulation average number of kink-pairs and the simulation average nucleation rate.	45
4.7	Obtained velocity for $p = 0.2$, $q = 2$, $T = 400 \text{ K}$ and $\tau = 50 \text{ MPa}$. The predicted velocity is that based on the initial rate.	48